Regional deformation and offshore crustal local faulting as combined processes to explain uplift through time constrained by investigating differentially-uplifted Late Quaternary palaeoshorelines: the foreland Hyblean Plateau, SE Sicily.

M. Meschis[1]*, G. Scicchitano[2], G.P. Roberts[1], J. Robertson[1], G. Barreca[3,4,5], C. Monaco[3,4,5], C. Spampinato[6], D. Sahy[7], F. Antonioli[8] , Z. K. Mildon[9], G. Scardino[2]

1. Department of Earth and Planetary Sciences, Birkbeck, University of London, London, UK
2. Dipartimento di Scienze della Terra e Geoambientali, Università degli Studi di Bari Aldo Moro, 70121 Bari, Italy
3. Dipartimento di Scienze Biologiche, Geologiche e Ambientali, University of Catania, Catania, Italy
4. CRUST-Centro inteRUniversitario per l'analisi SismoTettonica tridimensionale con applicazioni territoriali, Chieti, Italy
5. Istituto Nazionale di Geofisica e Vulcanologia (INGV-OE), Catania, Italy
6. Portable Lab Geology and Engineering s.r.l – Academic Spinoff University of Catania, Catania, Italy
7. British Geological Survey, Keyworth, NG12 5GG, United Kingdom
8. Laboratorio Modellistica Climatica e Impatti, Centro Ricerche Casaccia, ENEA, Rome, Italy
9. School of Geography, Earth and Environmental Sciences, University of Plymouth, Plymouth, UK

*****Corresponding author, email address: marco.meschis.14@ucl.ac.uk

Abstract

Quaternary uplift is well documented in SE Sicily, a region prone to damaging seismic events, such as the 1693 "Val di Noto" Earthquake (Mw 7.4), the largest seismic event reported within the Italian Earthquake Catalogue, whose seismogenic source is still debated and, consequently, the long-term seismic hazard is poorly-understood. However, the spatial variation in the timing and rates of uplift are still debated, so it is difficult to link the dominant tectonic process(es) responsible for the uplift and the location of seismogenic sources. To better constrain the uplift rate, we have refined the dating of Late Quaternary marine terraces, using a synchronous correlation approach, driven by both published and newly obtained numerical age controls ($^{234}U/^{230}Th$ dating on corals). This has allowed re-calculation of uplift rates along a N-S oriented transect within the Hyblean Plateau (HP) foreland region. Consequently, we have mapped the geometry of palaeoshorelines along a coastline-parallel transect, and hence the rates of uplift. The results suggest increasing uplift rate from south to north across the HP, and that uplift rates have remained constant through the late Quaternary. This spatially-changing but temporally constant uplift places constraints on the proportion of uplift produced by regional geodynamic processes versus produced by local faults, such as an offshore E-dipping active normal fault. We discuss these new findings in terms of the long-term seismic hazard for one of the most seismically-active regions in the Mediterranean Basin.

Key points:

Main point 1:

Differential uplift is mapped in the Hyblean Plateau (SE Sicily, Italy) by looking at raised palaeoshorelines over the Late Quaternary

Main point 2:

Differential uplift in the Hyblean Plateau is caused by a combined process between offshore normal faulting and regional processes

Main point 3:

Deformation rates associated to the offshore normal fault (Western Fault) need to be refined, subtracting the regional processes signal**.**

1. Introduction

The complexity of deformation in regions subject to a combination of collision, subduction, mantle flow, regional uplift, extension and volcanism leads to uncertainty in seismic hazard assessment and quantification of geodynamic processes. For example, the Hyblean Plateau (HP), SE Sicily in southern Italy lies in a zone of active convergence, south of Etna volcano, and close to offshore active normal faults. Quaternary uplift and active faulting in the HP is evidenced by a well-exposed sequence of raised marine terraces (Bianca et al., 1999; Monaco & Tortorici, 2000), and the occurrence of large earthquakes such as the 1693 "Val di Noto" Earthquake (Mw 7.4) (Guidoboni et al., 2007). However, the mechanism(s) producing these uplifted terraces, and the links between uplift, regional tectonics and local active faulting are still highly debated. In particular, previous studies have suggested that the uplift in the HP is (i) produced by the long-term of the faulting activity of a normal fault, so-called the Western Fault (Bianca et al., 1999) and (ii) interpreted as a positive flexural bulge at the front of the Sicilian chain produced by the orogenic load and the slab pull of the subducting Ionian slab (Billi et al., 2006; Cogan et al., 1989; Pedley & Grasso, 1992). This controversy needs to be addressed and new and refined crustal deformation rates can be the base for future works, investigating the region that hosted the earthquake with highest estimated magnitude (1693 Val di Noto Earthquake – M 7.4) within the Italian earthquake catalogue (Guidoboni et al., 2007).

This paper uses observations of the uplifted marine terraces to refine the chronology and spatial extent of the uplift. In particular, we map the inner edges of marine terraces, provide new estimated and refined ages for un-dated marine terraces and hence inner edges. This is done by applying a methodological approach so-called synchronous correlation technique, (i) driven by previous submerged palaeoshorelines knowledge (Dutton et al., 2009) and (ii) supported by new $^{234}U/^{230}Th$ dating. Overall, this produces a correlation between inner edge ages and ages of global glacio-eustatic sea-level highstands, useful to determine uplift rate scenarios that explain the observations. The results are used to discuss the relative influences of the doming effect from Mt. Etna located north of the HP (De Guidi et al., 2014), active normal faulting located offshore to the east (Argnani et al., 2012; Argnani & Bonazzi, 2005; Bianca et al., 1999; Monaco & Tortorici, 2000) and regional Africa-Eurasia collision/subduction processes including regional uplift associated with mantle flow (Barreca et al., 2016; Grad & Tiira, 2009; Neri et al., 2002; Westaway, 1993). We suggest that the ongoing uplift affecting the HP is related to a combined effect of prominent mantle flow/crustal thickening processes (e.g. Ferranti et al., 2006) and a less striking long-term footwall uplift from the offshore Western normal fault.

2. Geological background

The tectonic setting of SE Sicily is dominated by the ~N-S Neogene to Quaternary tectonic convergence between the European and African continental margins (Dewey et al., 1989; Faccenna et al., 2001). Progressive tectonic convergence has led to the formation of the Sicilian-Maghrebian chain and the Apennines, connected by the arc-shaped Calabrian Arc (Figure 1), which represents the sub-aerial portion of a larger accretionary prism in the Ionian Sea. It is the result of the Pliocene-Quaternary subduction of the Ionian realm, a 15-20 km thick crustal remnant (Catalano et al., 2001) of the Permo-Triassic "Neo-Tethys" ocean (Sengör, 1979). To the west, it is adjacent to the Pelagian Block (Ben-Avraham & Grasso, 1991; Nicolich et al., 2000; Torelli et al., 1998), which also includes the 25–30 km thick continental crustal portion of the HP in SE Sicily (Dellong et al., 2018, 2019). The transition from continental to oceanic material occurs along the Malta Escarpment in the near offshore of SE Sicily (Figure 1a), a Mesozoic passive margin which has been reactivated by oblique extension during the Quaternary (Hirn et al., 1997; Bianca et al., 1999).

The HP represents the onshore portion of a larger foreland domain, belonging to the Pelagian Block (Ben-Avraham & Grasso, 1991; Burollet et al., 1978; Cultrera et al., 2015; Grasso & Lentini, 1982). In particular, the HP, within the Hyblean-Malta Platform in the Central Mediterranean, represents a carbonate promontory of the larger African palaeo-margin (Grasso & Lentini, 1982). Geological and seismic studies have shown a six km thick Meso-Cenozoic sedimentary carbonate

succession with intercalated volcanic layers, which overlie the Palaeozoic basement; in places this carbonate succession has been overlain by Quaternary marine deposits associated with sequences of palaeoshorelines (Bianca et al., 1999; Lentini et al., 1987).

Neogene tectonic shortening has affected the northern margin of the Pelagian Block producing a NE-SW oriented SE-verging thrust and fold system to the north-west (the Sicilian Chain) and normal faulting on the HP (Cultrera et al., 2015; Grasso et al., 1995). Convergence to the north-west is currently accommodated by a regional-scale, northward deepening crustal seismogenic structure (named the Sicilian Basal Thrust SBT; Figure 1b) whose focal mechanisms are compatible with a nearly N-S shortening and with some field evidence of active folding and thrust deformation at the Sicilian chain front (Lavecchia et al., 2007). In particular, in the NW sector of Mt. Etna volcano the earthquakes reach a maximum depth of about 35 km (De Guidi et al., 2015; Lavecchia et al., 2007). Indeed, the northern rim of the HP, where the Scordia-Lentini Graben (SLG) is mapped (Figure 1a), is thought to be seismically active, yet it only partially accommodates (~ 50% of the total 10 mm/yr of convergence rate) the ongoing Africa-Eurasia convergence measured with the GPS system along a N-S oriented transect in SE Sicily (Chiarabba & Palano, 2017; DeMets et al., 2015; Ferranti et al., 2008; Mastrolembo Ventura et al., 2014; Mattia et al., 2012; Musumeci et al., 2014; Palano et al., 2012). This is also consistent, for instance, with the process of tectonic inversion mapped north of Augusta town within the SLG where extensional faults have been re-activated as high-angle thrust faults since 0.85 Ma (Mastrolembo Ventura et al., 2014; Mattia et al., 2012; Tortorici et al., 2006). For some, the seismogenic source of the 9th January 1693 Earthquake (Mw 6), interpreted as a foreshock of the 11th January 1693 Earthquake (Mw 7.4), could be located within the tectonically-inverted graben north of Augusta (Mastrolembo Ventura et al., 2014).

The tectonic evolution over the Quaternary of eastern Sicily has also involved crustal extension accommodated by normal faults. These include (i) the offshore Messina-Taormina Fault in the north, which produced the most damaging earthquakes recorded in Europe in the 20th and 21st century, such as the 1908 Messina Earthquake (M. 7.1) (e.g. Aloisi et al., 2013; Meschis et al., 2019 for review), and (ii) an E-dipping normal fault system located mostly offshore in the south (Argnani et al., 2012; Argnani & Bonazzi, 2005; Bianca et al., 1999); the HP lies in the footwall of this E-dipping normal fault system. Evidence for present-day activity on this E-dipping fault system includes basins infilled by synrift clastic wedges and marine Quaternary deposits that thicken towards the boundary faults (Argnani & Bonazzi, 2005; Bianca et al., 1999). For instance, one of the offshore faults, named the Western Fault, has been claimed to be the seismogenic source of the 1693 seismic event (see also Azzaro & Barbano, 2000; Jacques et al., 2001; Piatanesi & Tinti, 1998 among others), which is the highest magnitude earthquake reported within the official Italian Catalogue of Earthquakes (Guidoboni et al., 2007). Alternative suggested seismogenic sources for the 1693 "Val di Noto" Earthquake have been associated to (i) a segment of the S-verging, N-dipping Sicilian Basal Thrust at the front of the Apennine-Maghrebian chain (Lavecchia et al., 2007), (ii) two opposite-verging compressional faults at the front of the chain (INGV - DISS Working Group, 2018) and (iii) a portion the Ionian subduction plane (Gutscher et al., 2006).

Quaternary processes related to the interaction between sea level changes, regional uplift and crustal deformation have produced sequences of marine terraces mostly outcropping on the eastern part of the HP (Bianca et al., 1999; Monaco et al., 2002). Despite the paucity of numerically-dated palaeoshorelines and marine terrace deposits, previous geoscientists have attempted to investigate the uplift process affecting the HP by applying a "sequential" correlation approach, obtaining uplift rates of 0.65 mm/yr (Bianca et al., 1999). However, the "sequential" correlation approach may fail where age control is lacking, and low uplift rates may have allowed erosion of some palaeoshorelines. For instance, for the offshore Western Fault slip-rates > 3 mm/yr over the Late Quaternary have been suggested using the interpreted age of terraces carved within the onshore footwall in SE Sicily as age constraints (Bianca et al., 1999). However, these age estimates for palaeoshorelines may be affected by the overprinting problem (Pedoja et al., 2018; Meschis et al., 2018; Roberts et al., 2009; Roberts et al., 2013; Robertson et al., 2019), and further study and robust dating is required. Furthermore, the uplift was only attributed to the footwall uplift of the offshore Western Fault (Bianca et al., 1999).

In particular, a prominent sequence of uplifted Late Quaternary palaeoshorelines, is located between the Augusta peninsula in the north of the HP, to south of Syracuse town (Bianca et al., 1999). The ages of these palaeoshorelines have been poorly-constrained, due to the lack of absolute age

controls in the region, so uplift rates over the Late Quaternary have been uncertain. Furthermore, the "overprinting problem" occurs because Late Quaternary sea level highstands are not all exactly at the elevation of present sea level, and those lower than present sea level may have their palaeoshorelines destroyed by younger, higher sea levels, if uplift is not great enough to raise them above the wave-erosion zone. Thus, simply assigning the next highest palaeoshoreline to the next oldest sea level highstand age is prone to fail if some palaeoshorelines are not preserved (Meschis et al., 2018; Pedoja et al., 2018; Roberts et al., 2009; Roberts et al., 2013; Robertson et al., 2019), and this may be why the temporal and spatial pattern of uplift is still debated. Regardless of whether the uplift is related to the offshore crustal extension, regional processes, a combination of these, or the doming effect from Mt. Etna, previous studies show evidence of differential uplift within the HP (Antonioli et al., 2006; Bianca et al., 1999; Ferranti et al., 2006; Spampinato et al., 2011). However, it is still unclear if this uplift and the associated rates have been constant or fluctuating over the Late Quaternary, suggesting that more investigations are needed for an improved long-term seismic hazard assessment.

Furthermore, we highlight the existence of an under-utilised source of uplift-rate information. Constraints on the uplift rate can be gained by study of the ages of submerged palaeoshorelines offshore Syracuse town (Dutton et al., 2009) (Figure 2 for locations). Two submerged palaeoshorelines have been mapped at -20 m and -45 m under the present-day sea level. The ages of these palaeoshorelines have been constrained using $^{234}U/^{230}Th$ dating of calcite speleothems that grew subaerially during sea-level lowstands, and ^{14}C dating of layers of calcitic serpulids that encrusted the speleothems when the caves and speleothems were later flooded. These age constraints show that the shallower palaeoshoreline formed before 74 ka (Dutton et al., 2009). The deeper one at -45 m formed before 44 ka. In this paper, we will test whether using the above-mentioned numerical ages, allows these submerged palaeoshorelines to be assigned to the MIS 5.1 sea level highstand (76/80 ka, -20 m) and the MIS 3.3 sea level highstand (50 ka, -45 m).

2.1. Characteristics of the mapped uplift

This paper focusses on observations of uplift so an important starting point is to note that uplift varies on both long and short wavelengths within Southern Italy.

For example, evidence exists for long-wavelength uplift (Figure 1c), probably produced by mantle flow around the edges of the subducting slab at depth (Lucente et al., 2006), evidenced by observations of seismic tomography and seismic anisotropy. Significant regional uplift affects Calabria and NE Sicily, which progressively vanishes towards Apulia region to the north and HP to the south (Faccenna et al., 2011; Ferranti et al., 2006; Westaway, 1993). This large-scale topographic bulge, recorded by uplift and deformation of the MIS 5e terrace (125 ka) (Figure 1c; Ferranti et al., 2006), is suggested to originate from subcrustal mantle flow and spans a wider lithospheric area than the subducted Ionian slab underneath the southern Tyrrhenian Sea, which is traditionally claimed as the source for Calabria "regional" uplift (Faccenna et al., 2011; Gvirtzman & Nur, 2001; Westaway, 1993). As a consequence, it reaches a maximum rate above the Ionian subduction zone in southern and central Calabria with uplift rates > 1 mm/yr especially where the Ionian slab is detached (Barreca et al., 2016; Faccenna et al., 2011; Roberts et al., 2013; Scarfì et al., 2018), while lower uplift rates (decreasing to zero) are recorded in the Taranto Gulf and SE Sicily coast within the HP (Dutton et al., 2009; Ferranti et al., 2006).

On a shorter wavelength, uplift variations have been noted along the strike of active normal faults in Calabria and Sicily and others areas associated with subduction, due to displacement gradients along the faults (e.g. Ferranti et al., 2007; Giunta et al., 2012; Meschis et al., 2018; Roberts et al., 2013). For example, extension between the Ionian domain and the Hyblean-Malta block affects the region offshore the HP (Palano et al., 2012), where active extension is accommodated by E-dipping normal faults producing seismic events like the 1990 "Santa Lucia" earthquake (Mw 5.6) (Argnani & Bonazzi, 2005; Bianca et al., 1999; Monaco & Tortorici, 2000). Of particular importance here is the existence of a ~50 km-long, E-dipping normal fault, named Western Fault, mapped ~14-20 km offshore the investigated area, deforming Quaternary deposits and in places producing a fault scarp on the seafloor (Argnani et al., 2012; Argnani & Bonazzi, 2005). Some have hypothesized that this offshore fault may produce uplift within the HP (Bianca et al., 1999).

Thus, the combination of both long and short wavelength processes emphasises the need for robust constraints on the spatial and temporal variations in uplift across the HP if the relative contributions of different processes responsible for the uplift are to be ascertained.

3. Approach and Methods

In this section, we present how we approach our attempts to constrain and refine spatial and temporal variations in uplift across the HP, in order to find if this uplift is driven by one or multiple mechanisms. We describe the method for each step in the study in turn below.

3.1. DEM-based topographic analysis and field mapping of uplifted Late Quaternary palaeoshorelines

We have undertaken detailed GIS-based geomorphological analysis, by using 2 m high resolution DEM kindly provided by "*Regione Siciliana*" (Sicilian Region office), alongside field mapping of palaeoshorelines (Figure 2). Our DEM-based topographic analysis used the approach from previous studies of uplifted palaeoshorelines in the Mediterranean Basin (e.g. Meschis et al., 2018; Roberts et al., 2013; Robertson et al., 2019). We conducted new mapping of sites where previously mapped palaeoshorelines had been identified (Bianca et al., 1999), and in many locations confirmed the existence of prominent breaks of slope defining palaeoshoreline inner edges, both in the field and on the DEM, mapping these breaks of slope along strike wherever possible. Palaeoshoreline locations are predominantly palaeo-rocky shorelines, characterised by (i) flat-surfaces cut into bedrock by wave erosion, accompanied in places by shallow marine deposits lithified by early marine diagenesis (Meschis et al., 2018; Roberts et al., 2009; Roberts et al., 2013; Robertson et al., 2019), (ii) caves, lithophagid borings and notches at the up-dip terminations of wave-cut platforms (Ferranti et al., 2006; Firth & Stewart, 1996; Meschis et al., 2018; Roberts et al., 2013; Robertson et al., 2019), and (iii) millholes (or marine erosion pans) which are quasi-circular depressions developed on the wave-cut platform formed by the scouring action of pebbles as a result of wave action (Miller & Mason, 1994; Jennifer Robertson et al., 2019) (Figure 3). The combination of these three sets of features allowed us to interpret gently-sloping seaward surfaces as palaeoshoreface surfaces cut by wave-action and bounded up-dip by palaeo-sea-cliffs or rocky palaeoshorelines, following the lead of previous marine terrace investigations (Armijo et al., 1996; Bianca et al., 1999; Gallen et al., 2014; Meschis et al., 2018; Roberts et al., 2009, 2013) (Figure 3). We used a handheld GPS with a built-in barometric altimeter to constrain palaeoshoreline locations in terms of x, y and z coordinates. Once mapped along strike in GIS, we constructed 12 topographic profiles across the DEM to help visualize the geometry of the deformed palaeoshorelines and marine terrace deposits, marking locations on the profiles where palaeoshorelines were identified in the field (Figure 2).

Field mapping was crucial because some marine terraces and palaeoshorelines were clear on the DEM and in the field, but others were less clear to map on the DEM because detailed geomorphological fieldwork showed that (i) breaks of slope identified as palaeo-sea-cliffs were rather small in height above the sloping terraced surface (less or equal to few meters) and (ii) the geographic extent of the terrace surfaces and wave-cut platforms were limited (a few metres across) and too small to resolve on DEMs (Figure 3). In general, the combined approach of mapping of palaeoshoreline elevations from DEMs analysis and fieldwork allows a regional extensive coverage. Following the approach of previous studies (Meschis et al., 2018; Roberts et al., 2013; Robertson et al., 2019), regression analysis was applied to assess our mapping and correlations.

3.2. New $^{234}U/^{230}Th$ dating of corals

The fieldwork has involved sampling corals from marine terrace deposits for $^{234}U/^{230}Th$ dating (Figure 4). We identified a coral colony (*Cladocora caespitosa*) from a wave-cut platform at 14 m above sea-level, south of Syracuse and landward of the two dated submerged palaeoshorelines described by Dutton et al. (2009). Based on the position of the corals, we estimate that the colony formed on a substrate of lithified sub-wave base Quaternary bioclastic sands (calcarenite), and was bound by early marine cements, possibly at rising sea-level highstand/still-stand. Lithophagids bored during wave erosion at

highstand when the wave-cut platform formed (Figure 4). $^{234}U/^{230}Th$ dating was carried out at the Geochronology and Tracers Facility of the British Geological Survey, Keyworth, UK, using total dissolution methods outlined by Crémière et al. (2016), with isotope ratios measured on a Neptune Plus multi-collector inductively coupled plasma mass spectrometer (MC-ICP-MS). Preparation of coral samples was a crucial step before $^{234}U/^{230}Th$ analysis. Millimetre-scale corallite fragments were isolated from carefully selected and systematically cleaned sediment hand samples. Any material showing evidence of alteration and/or detrital matrix on the outside of the corallite wall was removed mechanically using a scalpel under a microscope and/or chemically by washing the wall with HCl (10%) for 5-10 seconds, followed by thorough rinsing with ultrapure water. Furthermore, coral septa were separated from the wall because they are thinner and more prone to diagenetic alteration processes (Roberts et al., 2009); only corallite walls were used for analysis in this paper. We also analysed both bulk corallite fragments (2 – 10 mg) and powder subsamples obtained using a computer-controlled drill equipped with a 200 μm drill bit in order to avoid any portion of the coral that showed discolouration or other evidence of alteration.

3.3. Synchronous correlation approach to assign ages to undated palaeoshorelines

In this paper, the synchronous correlation technique is adopted. This is based on the idea that sea-level highstands, producing marine terraces in uplifting regions (Lajoie, 1986), are not equally-spaced in time implying that the resultant marine terraces will not be equally-spaced in elevation for any given uplift-rate scenario (Meschis et al., 2018; Roberts et al., 2013; Robertson et al., 2019; Westaway, 1993). For example, if the uplift rate is constant, relative vertical distances between palaeoshorelines will be in phase with the relative time differences between glacio-eustatic sea-level highstands, but scaled differently, so simple iteration of the uplift-rate can be used to recover the uplift-rate that explains the observations through a best-fit approach. However, note that this approach also works if the uplift rate changes through time, because uplift rate changes can also be incorporated into the iteration (e.g. Roberts et al., 2009 for an example of this). Note, that for both constant and changing uplift rate scenarios, some palaeoshorelines may be overprinted and hence not preserved on an uplifting coastline. This occurs where palaeo-sea-level at a highstand was beneath the level of present-day sea-level due to a smaller global ocean volume at that time, combined with a low uplift-rate; these two factors combine so that a younger highstand with larger global ocean volume and higher palaeo-sea-level elevation overtops and erodes the older palaeoshoreline during sea-level rise. Note, that the synchronous correlation approach deals with this problem as all palaeoshoreline elevations are calculated and displayed on profiles, whereas sequential correlation is prone to fail in this scenario if the problem is not identified (e.g. see Roberts et al. 2009 for further explanation). Also, it is desirable to have at least one palaeoshoreline with age control in order to assume, as first step, a constant uplift rate through time and assess whether the iteratively-calculated sea-level highstand elevations match the elevations of measured and mapped palaeoshorelines. If they do not, then a different scenario involving changing uplift rate through time is investigated, iterating uplift rates driven by age controls, in order to find the best match with measured palaeoshoreline elevations. This approach was described in detail in Houghton et al. (2003), Roberts et al. (2009) and (2013), Meschis et al. (2018) and Robertson et al. (2019). Note that we have used sea level curves from Siddall et al. (2003) and Rohling et al. (2014) for our synchronous correlation approach (Table 1). However, some can argue that using different sea level curves can lead to obtain different final results for derived uplift rates. Yet, Robertson et al. (2019) shows that the use of other sea level curves (e.g. Waelbroeck et al., 2002) makes a minimum difference to retrieve rates of uplift.

To perform the synchronous correlation, topographic profiles are made intercepting the palaeoshorelines from DEM data (Figure 2). Then, using data from fieldwork to corroborate the topographic profile, interpretations are undertaken of the inner-edge elevations of palaeoshorelines (e.g. Meschis et al., 2018; Roberts et al., 2013; Robertson et al., 2019). Palaeoshoreline elevations from GIS analysis corroborated in the field are then input into a spreadsheet called the "Terrace Calculator" (Roberts et al., 2009, 2013). We start our modelling with an initial uplift rate scenario, constant through time, for each topographic profile, constrained by using one or more age controls for dated palaeoshorelines. This has allowed us the iteration of uplift rates in order to calculate the expected sea-level highstands elevations for un-dated palaeoshorelines and compare them to those measured on DEM

and in the field. Linear regression analysis, calculating the coefficient of determination R^2, quantifies the relationship between the predicted and measured palaeoshoreline elevations. In this paper, we iterate uplift rates, driven by age controls, aimed to find the best match between all mapped or "measured" uplifted palaeoshoreline elevations on a topographic profile and the "predicted" elevations which represent the sea level highstands from well-accepted and known sea level curves in the Late Quaternary (Rohling et al., 2014; Siddall et al., 2003) (Table 1), forcing the user to maximise the coefficient of determination (R^2 value) for a linear regression analysis through all palaeoshoreline elevation data. Error bars on this linear regression analysis are assigned considering that DEMs used from "Regione Siciliana" have a 2 m resolution, and the "predicted" elevations iteratively-calculated using well-known sea level curves (Rohling et al., 2014; Siddall et al., 2003) have 12 m of error on each sea level highstand. Furthermore, Root-Mean-Square (RMS) deviation calculations were conducted in order to identify the best fit and then the best uplift rate value. In particular, following an approach from previous studies (Meschis et al., 2018; Robertson et al., 2019), for each topographic profile precise values of uplift rates were gained by iterating values of uplift rates from 0 to 1 mm/yr at intervals of 0.05 mm/yr and plotting the RMS deviation values gained, from comparing the values of the measured/mapped versus predicted palaeoshoreline elevations (Figure 5).

3.4. Vertical deformation modelling to estimate the "footwall uplift" effect of the Western Fault

To investigate the possible influence of offshore normal faulting, and the role of possible footwall uplift of the Western Fault, we conducted elastic half-space modelling using *Coulomb 3.4* (Toda et al., 2011). We use the published trace of the fault which reveals changes in strike along the fault length (Argnani et al., 2012). The fault trace is incorporated into the modelling using the method and Coulomb software plug-in from Mildon et al., (2016), that uses the non-linear fault trace, with along strike bends, to produce a corrugated 3D fault surface. There is debate about the dip of the fault (Argnani et al., 2012; Bianca et al., 1999) and so we varied the modelled dip value between 30º (e.g. Argnani et al., 2012) and 70º (e.g. Bianca et al., 1999). We used a concentric slip distribution consistent with scaling relationships between fault length, earthquake magnitude and slip at depth and at the surface (Wells & Coppersmith, 1994), in order to obtain an earthquake magnitude ~ Mw 7 (we used a value of Mw 7.05). The implied uplift contours were then converted into uplift rate values over the Late Quaternary by assuming a value of 500 years for earthquake recurrence as suggested previously by some (Bianca et al., 1999) on the offshore Western Fault, as the historical record implies that ~Mw 7 events are unlikely to recur at < ~500 year intervals. Finally, we extracted the uplift rate field along the modern-day coastline to calculate the effect of footwall uplift on the mapped palaeoshorelines.

4. Results

Our mapping identified up to 12 palaeoshorelines, and some of these could be mapped along strike for many kilometres (Figures 2-9). However, note that in some areas we were unable to link palaeoshorelines along strike. Nonetheless, we suggest the palaeoshoreline locations and continuity along-strike we derived are similar to those published by others, confirming their mapping (e.g. Bianca et al. 1999), and adequate for our purposes. However, we conducted synchronous correlation to check and refine the ages for palaeoshorelines suggested by Dutton et al. (2009) and Bianca et al. (1999).

Figure 6a shows our attempt to correlate sea level highstands to submerged palaeoshorelines mapped by Dutton et al. (2009). In particular, these authors analysed a speleothem sampled in a cave carved within a submerged palaeocliff, identifying a sea level highstand, at -20 m and obtained an age of ~74 ka (Table 2) with a growth rate of ~ 10 cm/kyr which, while relatively rapid, is not unprecedented in the speleothem literature (e.g. Gascoyne et al., 1983; Goede & Vogel, 1991; Mickler et al., 2006; Musgrove et al., 2001; Niggemann et al., 2003). We stress that growth rates for speleothems can vary over 3-4 times of magnitude, with a range of 0.001 mm/yr and 1 mm/yr (100 cm/kyr) (Ford & Williams, 2007). These rates depend on several factors (local hydrology, soil/vegetation cover above the cave, airflow through the cave, etc.), suggesting that even within a single cave it is possible to have very different rates for different speleothems. It is important to note that some growth rates for speleothems from the Last Interglacial Maximum in southern Turkey and northern Italy (Corchia Cave) have been estimated around 40 cm/ky (Drysdale et al., 2009; Rowe et al., 2020). Therefore, it is plausible that

speleothems taken into account for this study started rapidly growing subaerially immediately after the sea level fall during the transition between MIS 5a sea level highstand (80.0 ka) and the successive lowstand, which shows the most rapid sea level fall of the Late Quaternary (Cutler et al., 2003). This suggests that the submerged palaeoshoreline at -20 m could belong to the MIS 5a (80.0 ka) sea level highstand and is here used as an age control (Table 2). It is important to note that the idea of assigning the -20 m submerged palaeoshoreline to the MIS 5a (80 ka) is supported by the fact that there is no striking evidence for this palaeoshoreline to be older and it is unlikely due to the overprinting problem. This is a common problem, when one works with raised palaeoshorelines in regions affected by relatively low uplift rates, recognized worldwide and in particular in the Mediterranean realm (e.g. Anderson et al., 1999; Caputo et al., 2010; Pedoja et al., 2018; Roberts et al., 2013; Robertson et al., 2019). For instance, Figure 6e shows that claiming an older age, as previously suggested of 175 ka (MIS 6d) (Dutton et al., 2009), is unlikely because of the overprinting problem. However, we cannot completely rule out the possibility that this submerged palaeoshoreline have not undergone a prominent and/or total overprinting process and thus it could be older, but more investigations would be needed. Likewise, a deeper cave carved within a submerged palaeocliff identifying a sea level highstand mapped at -45 m could belong to the MIS 3c (50 ka), given that the dated speleothem shows an age of 44 ka, as previously suggested (Dutton et al., 2009) (Table 2).

Using these elevations/depths and age control, we iterated values for uplift rates, using an initial "constant rate through time" scenario to find the best match between mapped palaeoshorelines, both offshore and onshore, and the predicted sea level highstand elevations. We find our preferred uplift rate of 0.18 mm/yr constant through time, a value in relatively close agreement with the 0.2 mm/yr suggested by Dutton et al. (2009) (Figure 6a). The robustness of our correlation is assessed by linear regression in Figure 6b where a coefficient of determination R^2 value >0.99 is found. Moreover, we calculate RMS deviation in order to find the best possible value of uplift rate as shown in Figure 6c, as proposed by previous studies (Meschis et al., 2018; Robertson et al., 2019). Figure 6d and the associated table show the sea level curve modelled using our preferred uplift rate, suggesting which sea level highstands and their predicted elevations will be preserved in the landscape. This is also supported by a new approximate age control from $^{230}Th/^{234}U$ dating on a coral sampled at 14 m in the same topographic profile (Profile 11) presented in Figure 6. Corals from this colony have proved to be difficult to date, as nine out of the ten analysed subsamples showed evidence of open system behaviour, i.e. U and/or Th exchange between the sample and its environment over time, to an extent that precludes age interpretation. The remaining sample gave an age of 102 ka, with an unusually low initial $\delta^{234}U$ value of 103.2‰ (Table 3) which appears to be consistent with precipitation form a mixture of seawater ($\delta^{234}U$ ~ 145‰) and the freshwater similar to that from which the speleothems analysed by Dutton et al. (2009) precipitated ($\delta^{234}U$ ~ 60‰). Furthermore, Table 3 shows a low value of U content (1.4 ppm), if compared to more reliable studies where U content for corals are close to 3 ppm (Dutton, 2015), suggesting for this paper U loss possibly due to leaching of U by freshwater. Although the calculation of the age gives ± 1.7 ky as error (Table 3), we think that the unusually low initial $\delta^{234}U$ value suggests that we should use this calculated age with caution. For instance, in the Gulf of Aqaba, raised palaeoshorelines have been investigated and by applying U/Th dating corals have been dated; some of them have shown low values of $\delta^{234}U$, and the calculated coral ages could actually be older as suggested by El-Asmar, (1997). This would suggest that our calculated coral age of 102 ka in this paper can be older and thus not ruling out the possibility that the actual coral age could be 119 ka. We thus use this approximate age of 102 ka to further substantiate our results from synchronous correlation. In particular, the synchronous correlation approach applied along the Profile 11 suggests that the 14 m high terrace also mapped by Bianca et al. (1999) in the field with a previously-proposed age of 60 ka must be older due to the existence of the approximate ~102 ka coral at this location. We are aware that our dated coral is not exactly at the elevation of the suggested sea level highstand (119 ka) but given the (i) uncertainty in the actual sea level curve ±12 m for each sea level highstand from Siddall et al. (2003) and Rohling et al. (2014),the fact that corals don't live exactly at sea level and the unusually low $\delta^{234}U$ value this coral age is consistent with the interpretation of 119 ka sea level highstand. In summary, the three palaeoshorelines can be explained with an uplift rate of 0.18 mm/yr, similar to that suggested by Dutton et al. (2009). Using this result as a guide, and by mapping the dated palaeoshorelines from Profile 11 along strike, we then used synchronous correlation on other profiles across the terraces to study the spatial and temporal pattern of uplift.

Figure 7 shows our synchronous correlation between palaeoshoreline elevations predicted by iterating values of uplift rate and palaeoshoreline elevations mapped in the field and on DEMs. Two criteria were applied when we iterated the uplift rates driven by available age controls (Table 2) and supported by new coral dating (Table 3), and the results from Profile 11 (Figure 6): (i) we sought to ensure that the clearest mapped palaeoshorelines were related to the most prominent sea-level highstands at 125, 240 and 340 ka; (ii) we attempted to maximize the coefficient of determination (R^2) to demonstrate how robustly other less prominent mapped palaeoshorelines match the iteratively-predicted palaeoshoreline elevations. This approach allows us to assign or in some cases re-evaluate for the first-time ages for mapped, but undated palaeoshorelines as shown in Table 4. To confirm that observations of the locations and elevations of palaeoshorelines made on the DEMs were robust and consistent with field measurements, we have produced a cross-plot showing a linear regression analysis used to measure R^2 values, with a value of >0.99, indicating a good correlation between palaeoshorelines measured in the field and palaeoshorelines measured on the DEMs. It is important to highlight that error bars on this linear regression analysis are assigned considering that DEMs used from "Regione Siciliana" have a 2 m resolution and palaeoshoreline elevations mapped in the field have errors of ± 3 m associated with the hand-held barometric altimeter. We checked the correlation between the DEMs-based topographic analysis and our mapped elevations in the field; we find that this correlation is robust within the margin of errors with $R^2 > 0.99$, suggesting that our "measured" elevations are reliable (Figure 8a). By linear regression analysis we assessed the robustness and reliability of the synchronous correlation approach between the "measured" palaeoshoreline elevations in the field and DEMs and the "predicted" elevations iteratively-calculated (Figure 8b), given (i) fixed values for sea-level relative to today for several highstands presented by Siddall et al. (2003) and Rohling et al. (2014) (Table 1) and (ii) an uplift rate driven by ages constraints. This correlation with R^2 value > 0.99 (Figure 8b) suggests that we have gained robust uplift-rate estimates for the HP region, implying that the uplift rate has been constant through time for the last half million years. Our results also show that the locations of our mapped palaeoshorelines are in very good agreement with those mapped by Bianca et al. (1999), yet, the suggested palaoeshoreline ages in that study needed revision. Another important result, as already proposed by previous studies investigating uplifted palaeoshorelines in the Mediterranean realm (Meschis et al., 2018; Roberts et al., 2013; Robertson et al., 2019), is that we have recognised and mapped palaeoshorelines linked to the sea-level highstands from 50, 76.5/80, 119, 125, 200, 240, 310, 340, 410, 478 and 525 ka (not all mapped within a single profile; Table 4). We stress that our refined chronology of palaeoshoreline ages and associated uplift rates in this study agrees with independent and previous studies (Antonioli et al., 2006; Dutton et al., 2009) for the same region.

Our interpretation of palaeoshorelines shows that uplift increases from south to north with tilted palaeoshorelines (Figure 9a) over the Late Quaternary. Differential uplift rates (Figure 9b) are derived, with higher values of uplift rates mapped in the north (0.41 mm/yr), with lower values in the south (0.16 mm/yr). Furthermore, we have investigated whether the tilted geometry of mapped palaeoshorelines developed sequentially through time or after all the terraces had been uplifted. If the tilting occurred gradually through time, older palaeoshorelines would show higher values of tilt angle. Figure 9c shows that older and higher mapped palaeoshorelines do indeed have higher values of tilt angle, suggesting that they have experienced a longer history of differential uplift, and that tilting was ongoing through the late Quaternary, and occurred progressively through time.

These interpretations showing differential uplift from north to south through time are in agreement with previous investigations for this area in terms of the locations and elevations of mapped palaeoshorelines (Bianca et al., 1999; Ferranti et al., 2006; Spampinato et al., 2011). However, the palaeoshorelines ages and hence uplift rates are not in agreement with these previous investigations.

In the next section, we discuss our results in terms of the relationships between the differential uplift we have mapped, and far-field geodynamic regional-scale processes and local "footwall uplift" produced by the activity of the offshore Western Fault.

5. Discussion

Our results suggest a constant uplift rate over the Late Quaternary, with the rate of uplift increasing from south to north (Figure 9a, b) within a foreland region represented by the HP. In this

section we discuss possible mechanisms that may explain the Late Quaternary uplift of the HP. Finally, presented results will be briefly discussed in terms of seismic hazard affecting the SE Sicily.

5.1. Fluctuating vs constant uplift rate through time

By applying a synchronous correlation approach, we suggest that a constant uplift rate through time provides the best match between multiple palaeoshorelines and multiple sea level highstands, and the limited age controls we have achieved with absolute dating (Figure 5, 6, 7 and 8). In other words, our best fit model achieves a close match to the geomorphology in terms of the elevations and number of palaeoshorelines, but call into doubt the reliability of the 102 ka coral age, which in any case has an unusually low initial $\delta^{234}U$ value (Table 3). We suggest this coral age is a useful approximation, albeit with likely diagenetic alteration of the sample, that nonetheless suggests the "Siracusa-Terrace" is older than 60 ka, the value previously proposed (Bianca et al., 1999 - yellow-coloured terrace in their Figure 4). Indeed, our refined chronology, with a constant uplift rate through time, suggests that this terrace should belong to the minor peak of the Last Interglacial Maximum (LIM) (119 ka) from north to south as shown in Figure 8 and Table 4. In this section, we briefly explore the possibility of using the potentially-altered coral age as a more precise age constraint, but show that we prefer a model that emphasises the good match between geomorphology and the model results over the reliability of the coral age. For instance, by applying our methodological approach on topographic profile 1, driven by the calculated coral age, we would assign the MIS 5c (100 ka) age to the 40 m mapped palaeoshoreline and claim a dramatic changing uplift rate through time (Supplement 1). In particular, to find the best match between multiple palaeoshoreline elevations and multiple sea level highstands, we would need to claim an uplift rate of 0.1 mm/yr before 100 ka and an uplift rate of 0.63 mm/yr after 100 ka. This would imply an unlikely uplift rate acceleration of x6 over a few ten thousand years (Supplement 2). Furthermore, this would also imply that one of the most common sea level highstand well-recorded and mapped throughout the Mediterranean area like the MIS 7e (240 ka), at 92 m mapped along Profile 1 (Figure 7 and Table 4) in this study, (Meschis et al., 2018; Roberts et al., 2009, 2013; Robertson et al., 2019) would not be recorded because it would be overprinted by the higher and younger LIM (125 ka) (Supplement 2a). Also, the RMS deviation, describing the best uplift rate value between the mapped geomorphology and the hypothesized model, calculated for this unlikely dramatic changing uplift rate scenario would be higher than the more likely "constant uplift rate" scenario claimed for this region. Because of the strong uncertainty affecting the calculated coral age due to the uncharacteristically low initial $\delta^{234}U$ value discussed in the previous section, we discard the dramatic "changing uplift rate" scenario for this area. We stress that in order to support an uplift rate acceleration, which would imply a drastic geodynamic change for the investigated area over a few ten thousand years, more reliable data and perhaps different absolute dating techniques to gain new knowledge on palaeoshoreline ages (e.g. Robertson et al., 2020) are needed. Thus, overall we prefer an interpretation of the uplift as occurring at a constant rate because it provides a good match with the geomorphology, with a lower RMS value (4.21), and is a simpler case in terms of tectonic processes. Yet, still take account of the coral age in that we use it to call into doubt the existing published age of the 40 m terrace.

5.2. Multiple components to explain HP uplift

According to previous works, uplift of the HP is due to footwall uplift over the Late Quaternary (Bianca et al., 1999; Monaco & Tortorici, 2000), and here we investigate whether offshore normal faults are close enough to the coast of the HP for this to be the case. It has been recognized that the effect of footwall uplift deformation decreases with distance from any given fault trace (DeMartini et al., 2004; Ward & Valensise, 1989). In particular, footwall uplift occurs for an across strike distance equal to about the half of the fault length. For instance, for the 1983 Borah Peak earthquake (Ms 7.2) on the Lost River Fault shows a co-seismic surface rupture of ~ 30 km length and an associated footwall uplift deformation of ~ 15 km into the footwall measured from its maximum displacement at the fault centre (Stein & Barrientos, 1985). Similarly, for the L'Aquila earthquake (Mw 6.2) the Paganica Fault produced a co-seismic surface rupture of ~ 24 km, with an associated footwall uplift deformation of ~ 12 km into the footwall measured from its maximum displacement at the fault centre (Papanikolaou et al., 2010). The most damaging and powerful earthquake recorded in Europe produced by a normal fault,

namely the Messina-Taormina Fault, shows a co-seismic rupture of ~ 58 km with an associated footwall uplift deformation of ~ 29 km into the footwall modelled from its maximum displacement at the fault centre (Meschis et al., 2019). Offshore of the investigated area, crustal extension accommodated by the E-dipping Western Fault (Argnani et al., 2012; Argnani & Bonazzi, 2005; Bianca et al., 1999) presents an entire length of ~ 50 km and is mapped between 14 and 20 km offshore of the investigated area. From the above, we would expect footwall uplift to extend 25 km into the footwall if the entire fault length ruptures. To test this, and quantify the magnitude of expected uplift, we modelled slip on the offshore mapped Western Fault in an elastic half-space using the Coulomb 3.4 software (Toda et al., 2011), applying a new Matlab code (Mildon et al., 2016) that allows us to include the mapped curvilinear fault trace and hence likely corrugated geometry of the fault plane. These combined codes allow us to model vertical and horizontal crustal movement produced by earthquakes on faults showing variable-strike geometry (Iezzi et al., 2018; Mildon et al., 2016; Toda et al., 2011), such as the co-seismic uplift and subsidence adjacent to the investigated fault (Figure 10). For this paper, we used fault parameters of a 50-km long E-dipping fault with a dip-angle of 70º (Bianca et al., 1999) and slip at depth of 5.5 m, at 5 km depth, with 10% of the slip maximum propagating to the surface, in order to obtain an earthquake magnitude of ~Mw 7.05. We also did the same with a fault dip of 30º. Our modelling reveals that a 70º dip-angle produces co-seismic footwall uplift affecting the eastern HP where uplifted palaeoshorelines are mapped (Figure 10a). A dip-angle of 30º produces quasi-zero uplift of the coast and hence was not investigated further (see Supplement 3). Furthermore, using the 70º dip angle, we calculated the uplift rate of the coastline, assuming the slip-rate and hence uplift-rate are constant over the last 525,000 years, by assuming a recurrence interval of 500 years, as previously proposed by some (Bianca et al., 1999). This recurrence interval of 500 years is likely to be close to a minimum plausible value, as more frequent recurrence would be recorded in the historical record and this is not the case (Guidoboni et al., 2007). The graph presented in Figure 10b shows that the long-term footwall uplift effect produces uplift rates that peak on the coast opposite the centre of the offshore fault but decreasing to the north and south. Thus, this does not explain the uplift increasing to the north, as described earlier in this paper. Furthermore, footwall uplift would produce only small part of the total magnitude of the uplift constrained by the uplifted palaeoshorelines given the earthquake recurrence interval we have assumed as a minimum value; additional uplift is required suggesting the existence of multiple processes contributing to the uplift.

Other explanations of uplift within NE Sicily and Calabria since Middle Pleistocene have been related to the Ionian subduction-collision and back-arc spreading processes associated mantle flow around south-eastward retreating Ionian slab (Barreca et al., 2016; Faccenna et al., 2011; Faccenna et al., 2004; Lucente et al., 2006; Scarfì et al., 2018) alongside isostatic rebound in response to slab detachment (Gvirtzman & Nur, 1999; Neri et al., 2012; Westaway, 1993). We noted that uplift and uplift rates measured in this paper (Figure 11 a and b) show higher values where higher depth values of the Moho discontinuity are mapped (Figure 11c). Moreover, recent geophysical investigations of the lithosphere show that slab detachment and mantle flow also occur north of the HP. Assuming that the effect of these processes vanishes towards the south, the correlation between deep-seated subcrustal processes and observed differential uplift could be consistent with the uplift mapped by Ferranti et al. (2006) and that mapped in this paper. Indeed, we note that Figure 12 shows a non-linear correlation between uplift rate and Moho depth with a power law exponent of ~1.86. This may suggest that viscous deformation is an important process in this area, because the relationship resembles that for viscous flow where driving stress raised to an exponent relates to the strain-rate (Cowie et al., 2013; Hirth et al., 2001; Shi et al., 2015). This may be related to viscous crustal or mantle flow due to slab processes or crustal thickening. Modelling to differentiate between these viscous processes is beyond the scope of this paper, but, in summary, we suggest for the first time, that viscous processes combined with the offshore Western Fault footwall uplift may control the uplift of the HP (Figure 10 and 11). Interestingly, similar combined mechanisms (regional processes and local contribution from faults) to explain crustal uplift, constrained by investigating raised palaeoshorelines, have been proposed for northern Calabria (Italy) (Santoro et al., 2013).

Finally, it can be argued that the crustal uplift in the northern rim of the HP could also be affected by the deep magmatic processes associated with the Etna volcano; however, taking into account the long-term magmatic source with the associated "doming effect" suggested by De Guidi et al. (2014), it is likely that the "doming effect" only provides a fraction of the total measured uplift (Figure 11d).

5.3. *Long-term seismic implications and future investigations*

We now turn to the question of whether we can use the uplift-rates we have described to help identify potential seismic sources.

Our discussion above suggests that normal faulting and associated footwall uplift could contribute to the measured uplift through the Quaternary. If the constant Quaternary uplift rate suggests a constant slip-rate through time on the offshore normal fault this may produce new insights into its associated seismic hazard. To gain actual values for the slip-rate on the normal fault one would have to subtract any uplift produced by regional processes. Otherwise, erroneous fault slip-rates and earthquake recurrence intervals will be derived for long-term seismic hazard assessment. This will be crucial if we consider that this fault (i) can produce damaging earthquakes with ~Mw 7 if the entire fault length is ruptured and (ii) cannot be ruled out as the seismogenic source of the 1693 "Val di Noto" earthquake (M 7.4). We, although, highlight that because the dominant signal of the uplift is from regional processes, we are aware that any possible small fluctuation on the slip-rate of the Western Fault over the Quaternary can have been overwhelmed by them. We stress that more investigations are needed to refine deformation rates associated to the Western Fault.

Also, it is important to highlight that the differential uplift we describe may well have been active through the Holocene. Vertical deformation studies within the HP have shown that higher Holocene uplift rates have been mapped close to Augusta town and the northern rim of the HP, and lower values have been mapped in the south around the location of Profile 10 (Scicchitano et al., 2008; Scicchitano et al., 2017; Spampinato et al., 2011) (Holocene uplift rates increase from 0.24 to 0.74 mm/yr from south to north; Figure 1). Moreover, a similar uplift gradient from north to south is recorded by GPS-based vertical movement investigations (Serpelloni et al., 2013). Although more detailed studies which cover the Holocene to present time are needed, this may suggest that (i) the ongoing Africa-Eurasia convergence (Figure 11e), and the offshore extensional Western Fault are seismically active processes that combine to produce constant rates through time, implying that more investigations are needed for a better (i) understanding of their relationship and (ii) seismic hazard approach.

6. Conclusions

In this paper, we use the synchronous correlation technique as methodological approach in order to refine ages for un-dated marine terraces. This allow us to refine uplift rates through time, overcoming the "overprinting problem" when we investigate regions affected by relatively low uplift rates such as the Hyblean Plateau (HP), SE Sicily. New rates of uplift constant through time spanning the Late Quaternary have been presented within the investigated area. By applying the synchronous correlation approach, driven by new age controls, a sequence of uplifted Late Quaternary marine terraces has been investigated. It has been shown that (i) palaeoshoreline elevations increase from south to north, (ii) higher uplift rates are mapped in the northern rim of the HP and (iii) their tilt angle shows higher values for the older and higher terraces. This suggests that regional geodynamics and long-term activity of the offshore Western Fault, were the combined cause of uplift, and have been constant through time. This highlights new insights for the long-term seismic hazard approach for one of the most seismically active regions in the Mediterranean Basin.

Acknowledgements

We thank Prof. Jonathan Aitchison, the Associate Editor, Luigi Ferranti and an anonymous reviewer for critically improving this manuscript with their comments.

This work was funded and supported by the London NERC DTP Scholarship (grant number reference: 1492238). $^{234}U/^{230}Th$ coral age dating was carried out at the Geochronology and Tracers Facility (BGS, UK) via grant IP-1734-0517. We thank "Regione Siciliana" for helping us to access the 2-m Digital Elevation Models. Dr. Mimmo Palano is thanked for providing the "Etna Doming Effect" data shown in Figure 11. All data for this paper are properly cited and referred to in the reference list and available on Figure 7, as topographic data where paleoshoreline elevations have been mapped, and in Table 4 (all mapped palaeoshoreline elevations and assigned ages). These data can be used to reproduce all results shown in Figures 8 and 9. I intend to place these data in a repository if the paper is accepted. Moho

depth shown on Figure 11 have been derived from https://www.seismo.helsinki.fi/mohomap/, with related publications properly cited in the Reference list.
They are also available by contacting the corresponding author (marco.meschis.14@ucl.ac.uk - marco.meschis@gmail.com).

Reference

Aloisi, M., Bruno, V., Cannavo, F., Ferranti, L., Mattia, M., & Monaco, C. (2013). Are the source models of the M 7.1 1908 Messina Straits earthquake reliable? Insights from a novel inversion and sensitivity analysis of levelling data" by Aloisi et al. (2012)'. *Geophysical Journal International*, *192*, 1025–1041. https://doi.org/https://doi.org/10.1093/gji/ggs062

Anderson, Densmore, & Ellis. (1999). The generation and degradation of marine terraces. *Basin Research*, *11*(1), 7–19. https://doi.org/10.1046/j.1365-2117.1999.00085.x

Antonioli, F., Kershaw, S., Renda, P., Rust, D., Belluomini, G., Cerasoli, M., et al. (2006). Elevation of the last interglacial highstand in Sicily (Italy): A benchmark of coastal tectonics. *Quaternary International*, *145–146*, 3–18. https://doi.org/10.1016/j.quaint.2005.07.002

Argnani, A., & Bonazzi, C. (2005). Malta Escarpment fault zone offshore eastern Sicily : Pliocene-Quaternary tectonic evolution based on new multichannel seismic data, *24*(Figure 1), 1–12. https://doi.org/10.1029/2004TC001656

Argnani, A., Armigliato, A., Pagnoni, G., Zaniboni, F., Tinti, S., & Bonazzi, C. (2012). Active tectonics along the submarine slope of south-eastern Sicily and the source of the 11 January 1693 earthquake and tsunami. *Natural Hazards and Earth System Science*, (2010), 1311–1319. https://doi.org/10.5194/nhess-12-1311-2012

Armijo, R., Meyer, B., King, G. C. P., Rigo, A., & Papanastassiou, D. (1996). Quaternary evolution of the Corinth Rift and its implications for the Late Cenozoic evolution of the Aegean. *Geophysical Journal International*, *126*(1), 11–53. https://doi.org/10.1111/j.1365-246X.1996.tb05264.x

Azzaro, R., & Barbano, M. S. (2000). Analysis of the seismicity of Southeastern Sicily: a proposed tectonic interpretation. *Annali Di Geofisica*, *43*(1), 171–188. https://doi.org/http://hdl.handle.net/2122/1292

Barreca, G., Scarfì, L., Cannavò, F., Koulakov, I., & Monaco, C. (2016). New structural and seismological evidence and interpretation of a lithospheric-scale shear zone at the southern edge of the Ionian subduction system (central-eastern Sicily, Italy). *Tectonics*, *35*(6), 1489–1505. https://doi.org/10.1002/2015TC004057

Ben-Avraham, Z., & Grasso, M. (1991). Crustal structure variations and transcurrent faulting at the eastern and western margins of the eastern Mediterranean. *Tectonophysics*, *196*(3–4), 269–277. https://doi.org/10.1016/0040-1951(91)90326-N

Bianca, M., Monaco, C., Tortorici, L., & Cernobori, L. (1999). Quaternary normal faulting in southeastern Sicily (Italy): a seismic source for the 1693 large earthquake. *Geophysical Journal International*, *139*(2), 370–394. https://doi.org/10.1046/j.1365-246x.1999.00942.x

Billi, A., Porreca, M., Faccenna, C., & Mattei, M. (2006). Magnetic and structural constraints for the noncylindrical evolution of a continental forebulge (Hyblea, Italy). *Tectonics*, *25*(3), n/a-n/a. https://doi.org/10.1029/2005TC001800

Burollet, P. F., Mugniot, J. M., & Sweeney, P. (1978). The Geology of the Pelagian Block: The Margins and Basins off Southern Tunisia and Tripolitania. In *The Ocean Basins and Margins* (pp. 331–359). Boston, MA: Springer US. https://doi.org/10.1007/978-1-4684-3039-4_6

Caputo, R., Bianca, M., & D'Onofrio, R. (2010). Ionian marine terraces of southern Italy: Insights into the Quaternary tectonic evolution of the area. *Tectonics*, *29*(4), n/a-n/a. https://doi.org/10.1029/2009TC002625

Catalano, R., Doglioni, C., & Merlini, S. (2001). On the Mesozoic Ionian Basin. *Geophysical Journal International*, *144*(1), 49–64. https://doi.org/10.1046/j.0956-540X.2000.01287.x

Cheng, H., Lawrence Edwards, R., Shen, C.-C., Polyak, V. J., Asmerom, Y., Woodhead, J., et al. (2013). Improvements in 230Th dating, 230Th and 234U half-life values, and U–Th isotopic measurements by multi-collector inductively coupled plasma mass spectrometry. *Earth and Planetary Science Letters*, *371–372*, 82–91. https://doi.org/10.1016/j.epsl.2013.04.006

Chiarabba, C., & Palano, M. (2017). Progressive migration of slab break-off along the southern Tyrrhenian plate boundary: Constraints for the present day kinematics. *Journal of Geodynamics*,

105, 51–61. https://doi.org/https://doi.org/10.1016/j.jog.2017.01.006
Cogan, J., Rigo, L., Grasso, M., & Lerche, I. (1989). Flexural tectonics of southeastern sicily. *Journal of Geodynamics*, *11*(3), 189–241. https://doi.org/10.1016/0264-3707(89)90007-0
Cowie, P. a., Scholz, C. H., Roberts, G. P., Faure Walker, J. P., & Steer, P. (2013). Viscous roots of active seismogenic faults revealed by geologic slip rate variations. *Nature Geoscience*, *3*(November), 10–14. https://doi.org/10.1038/ngeo1991
Crémière, A., Lepland, A., Chand, S., Sahy, D., Condon, D. J., Noble, S. R., et al. (2016). Timescales of methane seepage on the Norwegian margin following collapse of the Scandinavian Ice Sheet. *Nature Communications*, *7*(May), 11509. https://doi.org/10.1038/ncomms11509
Cultrera, F., Barreca, G., Scarfì, L., & Monaco, C. (2015). Fault reactivation by stress pattern reorganization in the Hyblean foreland domain of SE Sicily (Italy) and seismotectonic implications. *Tectonophysics*, *661*, 215–228. https://doi.org/10.1016/j.tecto.2015.08.043
Cutler, K. ., Edwards, R. ., Taylor, F. ., Cheng, H., Adkins, J., Gallup, C. ., et al. (2003). Rapid sea-level fall and deep-ocean temperature change since the last interglacial period. *Earth and Planetary Science Letters*, *206*(3–4), 253–271. https://doi.org/10.1016/S0012-821X(02)01107-X
Dellong, D., Klinglhoefer, F., Kopp, H., Graindorge, D., Margheriti, L., Moretti, M., et al. (2018). Crustal Structure of the Ionian Basin and Eastern Sicily Margin: Results From a Wide-Angle Seismic Survey. *Journal of Geophysical Research: Solid Earth*, *123*(3), 2090–2114. https://doi.org/10.1002/2017JB015312
Dellong, D., Klinglhoefer, F., Dannowski, A., Kopp, H., Murphy, S., Graindorge, D., et al. (2019). Geometry of the deep Calabrian subduction (Central Mediterranean Sea) from wide-angle seismic data and 3-D gravity modeling. *Geochemistry, Geophysics, Geosystems*. https://doi.org/https://doi.org/10.1029/2019GC008586
DeMartini, P. M., Pantosti, D., Palyvos, N., Lemeille, F., McNeill, L., & Collier, R. (2004). Slip rates of the Aigion and Eliki Faults from uplifted marine terraces, Corinth Gulf, Greece. *Comptes Rendus Geoscience*, *336*(4–5), 325–334. https://doi.org/10.1016/j.crte.2003.12.006
DeMets, C., Iaffaldano, G., & Merkouriev, S. (2015). High-resolution Neogene and Quaternary estimates of Nubia-Eurasia-North America Plate motion. *Geophysical Journal International*, *203*(1), 416–427. https://doi.org/10.1093/gji/ggv277
Dewey, J. F., Helman, M. L., Knott, S. D., Turco, E., & Hutton, D. H. W. (1989). Kinematics of the western Mediterranean. *Geological Society, London, Special Publications*, *45*(1), 265–283. https://doi.org/10.1144/GSL.SP.1989.045.01.15
Drysdale, R. N., Hellstrom, J. C., Zanchetta, G., Fallick, A. E., Sanchez Goni, M. F., Couchoud, I., et al. (2009). Evidence for Obliquity Forcing of Glacial Termination II. *Science*, *325*(5947), 1527–1531. https://doi.org/10.1126/science.1170371
Dutton, A. (2015). Uranium-thorium dating. In *Handbook of Sea-Level Research* (pp. 386–403). Chichester, UK: John Wiley & Sons, Ltd. https://doi.org/10.1002/9781118452547.ch26
Dutton, A., Scicchitano, G., Monaco, C., Desmarchelier, J. M., Antonioli, F., Lambeck, K., et al. (2009). Uplift rates defined by U-series and 14C ages of serpulid-encrusted speleothems from submerged caves near Siracusa, Sicily (Italy). *Quaternary Geochronology*, *4*(1), 2–10. https://doi.org/10.1016/j.quageo.2008.06.003
El-Asmar, H. (1997). Quaternary isotope stratigraphy and paleoclimate of coral reef terraces, Gulf of Aqaba, South Sinai, Egypt. *Quaternary Science Reviews*, *16*(8), 911–924. https://doi.org/10.1016/S0277-3791(96)00077-7
Faccenna, C., Funiciello, F., Giardini, D., & Lucente, P. (2001). Episodic back-arc extension during restricted mantle convection in the Central Mediterranean. *Earth and Planetary Science Letters*, *187*(1–2), 105–116. https://doi.org/10.1016/S0012-821X(01)00280-1
Faccenna, C., Molin, P., Orecchio, B., Olivetti, V., Bellier, O., Funiciello, F., et al. (2011). Topography of the Calabria subduction zone (southern Italy): Clues for the origin of Mt. Etna. *Tectonics*, *30*(1), 1–20. https://doi.org/10.1029/2010TC002694
Faccenna, Claudio, Piromallo, C., Crespo-Blanc, A., Jolivet, L., & Rossetti, F. (2004). Lateral slab deformation and the origin of the western Mediterranean arcs. *Tectonics*, *23*(1), n/a-n/a. https://doi.org/10.1029/2002TC001488
Ferranti, L., Antonioli, F., Mauz, B., Amorosi, A., Dai Pra, G., Mastronuzzi, G., et al. (2006). Markers of the last interglacial sea-level high stand along the coast of Italy: Tectonic implications.

Quaternary International, *145–146*, 30–54. https://doi.org/10.1016/j.quaint.2005.07.009
Ferranti, L., Monaco, C., Antonioli, F., Maschio, L., Kershaw, S., & Verrubbi, V. (2007). The contribution of regional uplift and coseismic slip to the vertical crustal motion in the Messina Straits, southern Italy: Evidence from raised Late Holocene shorelines. *Journal of Geophysical Research*, *112*(B6), B06401. https://doi.org/10.1029/2006JB004473
Ferranti, L., Oldow, J. S., D'Argenio, B., Catalano, R., Lewis, D., Marsella, E., et al. (2008). Active deformation in southern Italy, Sicily and southern Sardinia from GPS velocities of the peri-tyrrhenian geodetic array (PTGA). *Bollettino Della Societa Geologica Italiana*, *127*(2), 299–316.
Firth, C., & Stewart, I. (1996). Coastal elevation changes in eastern Sicily: implications for volcano instability at Mount Etna. *Geological Society, …*, (110), 153–167. https://doi.org/10.1144/GSL.SP.1996.110.01.12
Ford, D., & Williams, P. (2007). *Karst Hydrogeology and Geomorphology*. West Sussex, England: John Wiley & Sons Ltd,. https://doi.org/10.1002/9781118684986
Gallen, S. F., Wegmann, K. W., Bohnenstiehl, D. R., Pazzaglia, F. J., Brandon, M. T., & Fassoulas, C. (2014). Active simultaneous uplift and margin-normal extension in a forearc high, Crete, Greece. *Earth and Planetary Science Letters*, *398*, 11–24. https://doi.org/10.1016/j.epsl.2014.04.038
Gascoyne, M., Ford, D., & Schhwarcz, H. (1983). Rates of cave and landform development in the Yorkshire Dales from speleothem age data. *Earth Surface Processes & Landforms*, *8*, 557–568.
Giunta, G., Gueli, A. M., Monaco, C., Orioli, S., Ristuccia, G. M., Stella, G., & Troja, S. O. (2012). Middle-Late Pleistocene marine terraces and fault activity in the Sant'Agata di Militello coastal area (north-eastern Sicily). *Journal of Geodynamics*, *55*, 32–40. https://doi.org/10.1016/j.jog.2011.11.005
Goede, A., & Vogel, J. C. (1991). Trace element variations and dating of a Late Pleistocene Tasmanian speleothem, *88*, 121–131.
Grad, M., & Tiira, T. (2009). The Moho depth map of the European Plate. *Geophysical Journal International*, *176*(1), 279–292. https://doi.org/10.1111/j.1365-246X.2008.03919.x
Grasso, M., & Lentini, F. (1982). Sedimentary and tectonic evolution of the eastern Hyblean Plateau (southeastern Sicily) during late Cretaceous to Quaternary time. *Palaeogeography, Palaeoclimatology, Palaeoecology*, *39*(3–4), 261–280. https://doi.org/https://doi.org/10.1016/0031-0182(82)90025-6
Grasso, M., Miuccio, G., Maniscalco, R., Garofalo, P., La Manna, F., & Stamilla, R. (1995). Plio-Pleistocene structural evolution of the western margin of the Hyblean Plateau and the Maghrebian foredeep, SE Sicily. Implications for the deformational history of the Gela Nappe. *Annales Tectonicae*, *9*, 7–21.
De Guidi, G., Imposa, S., Scudero, S., & Palano, M. (2014). New evidence for Late Quaternary deformation of the substratum of Mt. Etna volcano (Sicily, Italy): clues indicate active crustal doming. *Bulletin of Volcanology*, *76*(5), 816. https://doi.org/10.1007/s00445-014-0816-8
De Guidi, G., Barberi, G., Barreca, G., Bruno, V., Cultrera, F., Grassi, S., et al. (2015). Geological, seismological and geodetic evidence of active thrusting and folding south of Mt. Etna (eastern Sicily): Revaluation of "seismic efficiency" of the Sicilian Basal Thrust. *Journal of Geodynamics*, *90*, 32–41. https://doi.org/10.1016/j.jog.2015.06.001
Guidoboni, E., Ferrari, G., Mariotti, D., Comastri, A., Tarabusi, G., & Valensise, G. (2007). Catalogue of Strong Earthquakes in Italy (461 BC-1997) and Mediterranean Area (760 BC-1500).
Gutscher, M.-A., Roger, J., Baptista, M.-A., Miranda, J. M., & Tinti, S. (2006). Source of the 1693 Catania earthquake and tsunami (southern Italy): New evidence from tsunami modeling of a locked subduction fault plane. *Geophysical Research Letters*, *33*(8), L08309. https://doi.org/10.1029/2005GL025442
Gvirtzman, Z., & Nur, A. (1999). Plate detachment, asthenosphere upwelling, and topography across subduction zones. *Geology*, *27*(6), 563. https://doi.org/10.1130/0091-7613(1999)027<0563:PDAUAT>2.3.CO;2
Gvirtzman, Z., & Nur, A. (2001). Residual topography, lithospheric structure and sunken slabs in the central Mediterranean. *Earth and Planetary Science Letters*, *187*(1–2), 117–130.

https://doi.org/10.1016/S0012-821X(01)00272-2
Hirth, G., Teyssier, C., & Dunlap, J. W. (2001). An evaluation of quartzite flow laws based on comparisons between experimentally and naturally deformed rocks. *International Journal of Earth Sciences*, *90*(1), 77–87. https://doi.org/10.1007/s005310000152
Houghton, S. L., Roberts, G. P., Papanikolaou, I. D., & McArthur, J. M. (2003). New 234 U- 230 Th coral dates from the western Gulf of Corinth: Implications for extensional tectonics. *Geophysical Research Letters*, *30*(19), 2013. https://doi.org/10.1029/2003GL018112
Iezzi, F., Mildon, Z., Walker, J. F., Roberts, G., Goodall, H., Wilkinson, M., & Robertson, J. (2018). Coseismic Throw Variation Across Along-Strike Bends on Active Normal Faults: Implications for Displacement Versus Length Scaling of Earthquake Ruptures. *Journal of Geophysical Research: Solid Earth*, 1–25. https://doi.org/10.1029/2018JB016732
INGV - DISS Working Group. (2018). Database of Individual Seismogenic Sources (DISS), Version 3.2.1: A compilation of potential sources for earthquakes larger than M 5.5 in Italy and surrounding areas. https://doi.org/10.6092/INGV.IT-DISS3.2.1
Jacques, E., Monaco, C., Tapponnier, P., Tortorici, L., & Winter, T. (2001). Faulting and earthquake triggering during the 1783 Calabria seismic sequence. *Geophysical Journal International*, *147*(3), 499–516. https://doi.org/10.1046/j.0956-540x.2001.01518.x
Lajoie, K. R. (1986). Coastal Tectonics. In *Active Tectonics: Impact on Society* (pp. 95–124). Retrieved from http://books.google.com/books?hl=en&lr=&id=qaz9KnE2lxQC&pgis=1
Lavecchia, G., Ferrarini, F., de Nardis, R., Visini, F., & Barbano, M. S. (2007). Active thrusting as a possible seismogenic source in Sicily (Southern Italy): Some insights from integrated structural–kinematic and seismological data. *Tectonophysics*, *445*(3–4), 145–167. https://doi.org/10.1016/j.tecto.2007.07.007
Lentini, F., Di Geronimo, I., Grasso, M., Carbone, S., Sciuto, F., Scamarda, G., et al. (1987). Carta geologica della Sicilia sud-orientale. Università di Catania, Istituto di Scienze della Terra, 1987. S.EL.CA. Ed, Florence.
Lucente, F. P., Margheriti, L., Piromallo, C., & Barruol, G. (2006). Seismic anisotropy reveals the long route of the slab through the western-central Mediterranean mantle. *Earth and Planetary Science Letters*, *241*(3–4), 517–529. https://doi.org/10.1016/j.epsl.2005.10.041
Mastrolembo Ventura, B., Serpelloni, E., Argnani, A., Bonforte, A., Bürgmann, R., Anzidei, M., et al. (2014). Fast geodetic strain-rates in eastern Sicily (southern Italy): New insights into block tectonics and seismic potential in the area of the great 1693 earthquake. *Earth and Planetary Science Letters*, *404*, 77–88. https://doi.org/10.1016/j.epsl.2014.07.025
Mattia, M., Bruno, V., Cannavò, F., & Palano, M. (2012). Evidences of a contractional pattern along the northern rim of the Hyblean plateau (Sicily, Italy) from GPS data. *Geologica Acta*, *10*(1), 63–70. https://doi.org/10.1344/105.000001705
Meschis, M., Roberts, G. P., Robertson, J., & Briant, R. M. (2018). The Relationships Between Regional Quaternary Uplift, Deformation Across Active Normal Faults, and Historical Seismicity in the Upper Plate of Subduction Zones: The Capo D'Orlando Fault, NE Sicily. *Tectonics*, *37*(5), 1231–1255. https://doi.org/10.1029/2017TC004705
Meschis, M, Roberts, G. P., Mildon, Z. K., Robertson, J., Michetti, A. M., & Faure Walker, J. P. (2019). Slip on a mapped normal fault for the 28 th December 1908 Messina earthquake (Mw 7.1) in Italy. *Scientific Reports*, (April), 1–8. https://doi.org/10.1038/s41598-019-42915-2
Mickler, P. J., Stern, L. A., Banner, J. L., Cave, H., & Only, W. I. (2006). Large kinetic isotope effects in modern speleothems, (1), 65–81. https://doi.org/10.1130/B25698.1
Mildon, Z. K., Toda, S., Faure Walker, J. P., & Roberts, G. P. (2016). Evaluating models of Coulomb stress transfer: Is variable fault geometry important? *Geophysical Research Letters*, *43*(24), 12,407-12,414. https://doi.org/10.1002/2016GL071128
Miller, W. R., & Mason, T. R. (1994). Erosional Features of Coastal Beachrock and Aeolianite Outcrops in Natal and Zululand, South Africa. *Journal of Coastal Research*, *10*(2), 374–394. https://doi.org/10.2307/4298223
Monaco, C., Bianca, M., Catalano, S., De Guidi, & Tortorici, L. (2002). Sudden change in the Late Quaternary tectonic regime in eastern Sicily : evidences from geological and geomorphological features. *Bollettino Della Societa Geologica Italiana*, *1*(January), 901–913.
Monaco, Carmelo, & Tortorici, L. (2000). Active faulting in the Calabrian arc and eastern Sicily.

Journal of Geodynamics, *29*(3–5), 407–424. https://doi.org/10.1016/S0264-3707(99)00052-6
Musgrove, M., Banner, J. L., Mack, L. E., Combs, D. M., James, E. W., & Edwards, R. L. (2001). Geochronology of late Pleistocene to Holocene speleothems from central Texas : Implications for regional paleoclimate, (12), 1532–1543. https://doi.org/https://doi.org/10.1130/0016-7606(2001)113<1532:GOLPTH>2.0.CO;2
Musumeci, C., Scarfì, L., Palano, M., & Patanè, D. (2014). Foreland segmentation along an active convergent margin: New constraints in southeastern Sicily (Italy) from seismic and geodetic observations. *Tectonophysics*, *630*(C), 137–149. https://doi.org/10.1016/j.tecto.2014.05.017
Neri, G., Barberi, G., Orecchio, B., & Aloisi, M. (2002). Seismotomography of the crust in the transition zone between the southern Tyrrhenian and Sicilian tectonic domains. *Geophysical Research Letters*, *29*(23), 50-1-50–4. https://doi.org/10.1029/2002GL015562
Neri, G., Marotta, A. M., Orecchio, B., Presti, D., Totaro, C., Barzaghi, R., & Borghi, A. (2012). How lithospheric subduction changes along the Calabrian Arc in southern Italy: geophysical evidences. *International Journal of Earth Sciences*, *101*(7), 1949–1969. https://doi.org/10.1007/s00531-012-0762-7
Nicolich, R., Laigle, M., Hirn, A., Cernobori, L., & Gallart, J. (2000). Crustal structure of the Ionian margin of Sicily: Etna volcano in the frame of regional evolution. *Tectonophysics*, *329*(1–4), 121–139. https://doi.org/10.1016/S0040-1951(00)00192-X
Niggemann, S., Mangini, A., Richter, D. K., & Wurth, G. (2003). A paleoclimate record of the last 17600 years in stalagmites from the, *22*, 555–567.
Palano, M., Ferranti, L., Monaco, C., Mattia, M., Aloisi, M., Bruno, V., et al. (2012). GPS velocity and strain fields in Sicily and southern Calabria, Italy: Updated geodetic constraints on tectonic block interaction in the central Mediterranean. *Rendiconti Online Societa Geologica Italiana*, *21*(PART 1), 235–237. https://doi.org/10.1029/2012JB009254
Papanikolaou, I., Roberts, G., Foumelis, M., Parcharidis, I., & Lekkas, E. (2010). The Fault Geometry and Surface Ruptures , the Damage Pattern and the Deformation Field of the 6th and 7th of April 2009 , Mw = 6 . 3 and Mw = 5 . 6 Earthquakes in L ' Aquila (Central Italy) Revealed by Ground and Space Based Observations, *12*, 73–87.
Pedley, M. H., & Grasso, M. (1992). Miocene syntectonic sedimentation along the western margins of the Hyblean-Malta platform: A guide to plate margin processes in the central Mediterranean. *Journal of Geodynamics*, *15*(1–2), 19–37. https://doi.org/10.1016/0264-3707(92)90004-C
Pedoja, K., Jara-Muñoz, J., De Gelder, G., Robertson, J., Meschis, M., Fernandez-Blanco, D., et al. (2018). Neogene-Quaternary slow coastal uplift of Western Europe through the perspective of sequences of strandlines from the Cotentin Peninsula (Normandy, France). *Geomorphology*, *303*, 338–356. https://doi.org/10.1016/j.geomorph.2017.11.021
Piatanesi, A., & Tinti, S. (1998). A revision of the 1693 eastern Sicily earthquake and tsunami. *Journal of Geophysical Research: Solid Earth*, *103*(B2), 2749–2758. https://doi.org/10.1029/97JB03403
Roberts, G. P., Houghton, S. L., Underwood, C., Papanikolaou, I., Cowie, P. A., van Calsteren, P., et al. (2009). Localization of Quaternary slip rates in an active rift in 10 5 years: An example from central Greece constrained by 234 U- 230 Th coral dates from uplifted paleoshorelines. *Journal of Geophysical Research*, *114*(B10), B10406. https://doi.org/10.1029/2008JB005818
Roberts, G. P., Meschis, M., Houghton, S., Underwood, C., & Briant, R. M. (2013). The implications of revised Quaternary palaeoshoreline chronologies for the rates of active extension and uplift in the upper plate of subduction zones. *Quaternary Science Reviews*, *78*, 169–187. https://doi.org/10.1016/j.quascirev.2013.08.006
Robertson, J., Roberts, G. P., Iezzi, F., Meschis, M., Gheorghiu, D. M., Sahy, D., et al. (2020). Distributed normal faulting in the tip zone of the South Alkyonides Fault System, Gulf of Corinth, constrained using 36Cl exposure dating of late-Quaternary wave-cut platforms. *Journal of Structural Geology*, *136*(April), 104063. https://doi.org/10.1016/j.jsg.2020.104063
Robertson, J., Meschis, M., Roberts, G. P., Ganas, A., & Gheorghiu, D. (2019). Temporally constant Quaternary uplift rates and their relationship with extensional upper-plate faults in south Crete (Greece), constrained with 36-Cl cosmogenic exposure dating. *Tectonics*.
Rohling, E. J., Foster, G. L., Grant, K. M., Marino, G., Roberts, A. P., Tamisiea, M. E., & Williams, F. (2014). Sea-level and deep-sea-temperature variability over the past 5.3 million years. *Nature*,

508(7497), 477–482. https://doi.org/10.1038/nature13230
Rowe, P. J., Wickens, L. B., Sahy, D., Marca, A. D., Peckover, E., Noble, S., et al. (2020). Multi-proxy speleothem record of climate instability during the early last interglacial in southern Turkey. *Palaeogeography, Palaeoclimatology, Palaeoecology*, *538*(October 2019), 109422. https://doi.org/10.1016/j.palaeo.2019.109422
Santoro, E., Ferranti, L., Burrato, P., Mazzella, M. E., & Monaco, C. (2013). Deformed Pleistocene marine terraces along the Ionian Sea margin of southern Italy: Unveiling blind fault-related folds contribution to coastal uplift. *Tectonics*, *32*(3), 737–762. https://doi.org/10.1002/tect.20036
Scarfì, L., Barberi, G., Barreca, G., Cannavò, F., Koulakov, I., & Patanè, D. (2018). Slab narrowing in the Central Mediterranean: the Calabro-Ionian subduction zone as imaged by high resolution seismic tomography. *Scientific Reports*, *8*(1), 5178. https://doi.org/10.1038/s41598-018-23543-8
Scicchitano, G., Berlinghieri, E. F. C., Antonioli, F., Spampinato, C. R., & Monaco, C. (2017). Sacred Landscapes and Changing Sea Levels: New Interdisciplinary Data from the Early Neolithic to the Present in South-Eastern Sicily. In *Under the Sea: Archaeology and Palaeolandscapes of the Continental Shelf* (pp. 233–253). https://doi.org/https://doi.org/10.1007/978-3-319-53160-1_16
Scicchitano, Giovanni, Antonioli, F., Berlinghieri, E. F. C., Dutton, A., & Monaco, C. (2008). Submerged archaeological sites along the Ionian coast of southeastern Sicily (Italy) and implications for the Holocene relative sea-level change. *Quaternary Research*, *70*(1), 26–39. https://doi.org/https://doi.org/10.1016/j.yqres.2008.03.008
Sengör, A. M. C. (1979). Mid-Mesozoic closure of Permo–Triassic Tethys and its implications. *Nature*, *279*(5714), 590–593. https://doi.org/10.1038/279590a0
Serpelloni, E., Faccenna, C., Spada, G., Dong, D., & Williams, S. D. P. (2013). Vertical GPS ground motion rates in the Euro-Mediterranean region: New evidence of velocity gradients at different spatial scales along the Nubia-Eurasia plate boundary. *Journal of Geophysical Research: Solid Earth*, *118*(11), 6003–6024. https://doi.org/10.1002/2013JB010102
Shi, F., Zhang, J., Xia, G., Jin, Z., & Green, H. W. (2015). Rheology of Mg 2 GeO 4 olivine and spinel harzburgite: Implications for Earth's mantle transition zone. *Geophysical Research Letters*, *42*(7), 2212–2218. https://doi.org/10.1002/2015GL063316
Siddall, M., Rohling, E. J., Almogi-Labin, A., Hemleben, C., Meischner, D., Schmelzer, I., & Smeed, D. A. (2003). Sea-level fluctuations during the last glacial cycle. *Nature*, *423*(6942), 853–858. https://doi.org/10.1038/nature01690
Spampinato, C. R., Costa, B., Di Stefano, A., Monaco, C., & Scicchitano, G. (2011). The contribution of tectonics to relative sea-level change during the Holocene in coastal south-eastern Sicily: New data from boreholes. *Quaternary International*, *232*(1–2), 214–227. https://doi.org/10.1016/j.quaint.2010.06.025
Stein, R. S., & Barrientos, S. E. (1985). Planar high-angle faulting in the basin and range: Geodetic analysis of the 1983 Borah Peak, Idaho, earthquake. *Journal of Geophysical Research*, *90*(B13), 11355. https://doi.org/10.1029/JB090iB13p11355
Toda, S., Stein, R. S., Sevilgen, V., & Lin, J. (2011). Coulomb 3.3. Graphic-rich deformation & stress-change software for earthquake, tectonic and volcano research and teaching - User Guide. *USGS Open-File Report*, 63. Retrieved from https://pubs.usgs.gov/of/2011/1060/
Torelli, L., Grasso, M., Mazzoldi, G., & Peis, D. (1998). Plio–Quaternary tectonic evolution and structure of the Catania foredeep, the northern Hyblean Plateau and the Ionian shelf (SE Sicily). *Tectonophysics*, *298*(1–3), 209–221. https://doi.org/10.1016/S0040-1951(98)00185-1
Tortorici, G., De Guidi, G., & Sturiale, G. (2006). Evoluzione tettonica quaternaria del margine settentrionale del Plateau Ibleo (Sicilia sud-orientale). *Bollettino Della Societa Geologica Italiana*, *125*(1), 21–37.
Waelbroeck, C., Labeyrie, L., Michel, E., Duplessy, J. C., McManus, J. F., Lambeck, K., et al. (2002). Sea-level and deep water temperature changes derived from benthic foraminifera isotopic records. *Quaternary Science Reviews*, *21*(1–3), 295–305. https://doi.org/10.1016/S0277-3791(01)00101-9
Ward, S. N., & Valensise, G. (1989). Fault parameters and slip distribution of the 1915 Avezzano, Italy, earthquake derived from geodetic observations. *Bulletin of the Seismological Society of America*, *79*(3), 690–710.
Wells, D. L., & Coppersmith, K. J. (1994). New empirical relationships among magnitude, rupture

length, rupture width, rupture area, and surface displacement. *Bulletin of the Seismological Society of America*, *84*(4), 974–1002. Retrieved from http://www.bssaonline.org/content/84/4/974.short

Westaway, R. (1993). Quaternary uplift of southern Italy. *Journal of Geophysical Research*, *98*(B12), 741–772. https://doi.org/10.1029/93JB01566

Table 1

Age (ka)	Elevation of highstands (mm)
0	0
30	-80000
50	-60000
76.5/80	-30000
100	-25000
115	-21000
119	-5000
125	5000
175	-30000
200	-5000
217	-30000
240	-5000
285	-30000
310	-22000
340	5000
410	-5000
478	0

525	20000
550	10000
560	3000
590	20000
620	20000
695	10000
740	5000
800	20000
855	20000
980	25000

Table 1: *Values of sea-level highstands derived from Siddall et al. (2003) and Rohling et al., (2014) used to calculate predicted palaeoshoreline elevations given a value for uplift rate.*

Table 2

Reference	Dating Method	Dated sample description	Profile number	Assigned Highstand (ka)	Palaeo-shoreline Elevation (m a.s.l)
Dutton et al., 2009	U/Th	*"Three specimens of stalagmite."*	12	76.5/80	-20
Dutton et al., 2009	U/Th	*"A specimen of stalactite."*	12	50	-45

Table 2: *Age controls derived from two submerged palaeoshorelines available in the literature. Locations are shown in Figure 2.*

Table 3

Sample	Weight (mg)	U (ppm)	Th (ppm)	(^{230}Th/^{232}Th)	(^{232}Th/^{238}U)	(^{230}Th/^{238}U)	(^{234}U/^{238}U)	Age (ka)	$\delta^{234}U_i$	Assigned age (ka)
18	3.18	1.09	0.108	40.0	0.03246 ± 0.00004	1.299 ± 0.004	1.096 ± 0.003	-	-	-
19	4.03	1.11	0.181	22.7	0.05372 ± 0.00005	1.221 ± 0.004	1.097 ± 0.002	-	-	-

20A	3.96	0.94	0.167	22.5	0.05861 ± 0.00007	1.320 ± 0.004	1.104 ± 0.003	-	-	-
20B	0.46	0.85	0.027	142.4	0.01042 ± 0.00002	1.484 ± 0.013	1.107 ± 0.008	-	-	-
20C	0.19	0.68	0.107	34.2	0.05185 ± 0.00039	1.774 ± 0.027	1.136 ± 0.016	-	-	-
20D	0.25	0.29	0.159	16.2	0.17930 ± 0.00257	2.908 ± 0.067	1.023 ± 0.027	-	-	-
21A	10.0	0.93	0.324	11.2	0.11412 ± 0.00007	1.281 ± 0.003	1.102 ± 0.002	-	-	-
21B	1.24	0.73	0.033	117.2	0.01458 ± 0.00002	1.709 ± 0.013	1.109 ± 0.006	-	-	-
21C	0.67	1.40	0.020	142.6	0.00465 ± 0.00001	0.662 ± 0.005	1.108 ± 0.006	102.0 ± 1.7	103 ± 8	119 (?)
21D	0.54	0.64	0.053	61.1	0.02754 ± 0.00007	1.684 ± 0.020	1.134 ± 0.009	-	-	-

Table 3: *Measurements of U/Th isotope ratios of a coral sample collected near Syracuse town. The location of the collected corals is shown in Figure 2. Activity ratios were corrected for instrumental effects (mass bias, secondary electron multiplier versus Faraday cup yield, and hydride formation and tailing) and the contribution of naturally-occurring U and Th isotopes from the ^{229}Th-^{236}U isotopic tracer, and were calculated using the decay constants of Cheng et al. (2013). Age and initial δ^{234}U were calculated assuming an initial detrital (^{232}Th/^{238}U) of 1.2 ± 0.6 with secular equilibrium in the ^{238}U decay chain. All uncertainties are quoted at the 2-sigma level.*

Table 4

Profile (Sea level highstand referred to Figure 2)	UTM Coordinate (Easting)	UTM Coordinate (Northing)	DEMs Elevations (m)	Expected Elevations (m)	Our proposed Age (ky)	Age proposed by Bianca et al., 1999 (ky)	Barometric altimeter palaeoshoreline elevations (this study) (m)
1 (3a)	0511798	4128664	40	44	119	60	32
1 (3)	0511552	4128355	53	56	125	80	-
1 (5)	0510992	4127423	73	77	200	-	-
1 (7)	0510876	4127282	92	93	240	100	-
1 (9)	0510678	4127069	110	105	310	-	-
1 (10)	0509179	4125651	143	144	340	125	-
1 (11)	0507622	4124802	164	163	410	-	-
1 (12)	0506230	4124048	205	196	478	200	-
1 (13)	0505295	4123550	235	235	525	240	-
2 (3a)	0515345	4119964	30	38	119	60	-
2 (3)	0514217	4120518	48	50	125	80	-
2 (7)	0512863	4121361	78	81	240	100	-
2 (9)	0512577	4121369	89	90	310	-	-
2 (10)	0511095	4121342	124	127	340	125	-
2 (11)	0509086	4121288	149	143	410	-	-
2 (12)	0508187	4121081	180	172	478	200	-
3 (3a)	0514208	4118690	33	35	119	60	-
3 (3)	0513463	4118739	45	48	125	80	-
3 (5)	0512975	4118790	63	63	200	-	-
3 (7)	0512874	4118797	80	77	240	100	-
3 (9)	0512465	4118832	87	83	310	-	-
3 (10)	0511617	4118857	114	121	340	125	-
3 (11)	0510498	4118726	142	134	410	-	-

3 (12)	0509978	4118590	157	163	478	200	-
3 (13)	0509238	4118419	198	199	525	240	205
4 (3a)	0515954	4115491	25	31	119	60	
4 (3)	0515706	4115434	41	43	125	80	-
4 (7)	0515298	4115351	64	67	240	100	-
4 (9)	0514853	4115267	79	71	310	-	-
4 (10)	0513649	4115181	115	107	340	125	-
4 (11)	0513067	4115071	120	118	410	-	-
4 (12)	0512748	4114826	135	143	478	200	-
4 (13)	0512365	4114546	172	178	525	240	-
3a (5)	0516074	4114009	28	30	119	60	-
3 (5)	0515745	4113944	40	41	125	80	-
7 (5)	0514956	4113539	66	65	240	100	-
10 (5)	0514144	4113529	96	104	340	125	-
12 (5)	0513225	4113844	135	139	478	200	133
13 (5)	0512742	4113972	175	172	525	240	180
6 (3a)	0516603	4112325	30	28	119	60	-
6 (3)	0516210	4111940	40	40	125	80	37
6 (5)	0516074	4111853	51	51	200	-	-
6 (7)	0515909	4111750	60	62	240	100	-
6 (10)	0514740	4111378	105	100	340	125	-
6 (12)	0514325	4111194	134	134	478	200	137
6 (13)	0513822	4110995	165	167	525	240	175
7 (3a)	0520284	4107458	20	21	119	60	-
7 (3)	0520014	4107098	33	33	125	80	34
7 (5)	0519936	4107052	36	39	200	-	-
7 (7)	0519682	4106913	48	48	240	100	50
7 (10)	0519037	4106554	80	80	340	125	87
7 (12)	0518482	4106306	105	105	478	200	102
7 (13)	0517809	4106154	137	136	525	240	134
8 (3a)	0526586	4105288	18	20	119	60	27
8 (3)	0526126	4105231	32	31	125	80	36
8 (7)	0525975	4105215	50	45	240	100	43
8 (10)	0523251	4104783	76	76	340	125	-
8 (11)	0521890	4104843	86	81	410	-	-
8 (12)	0521306	4104935	98	100	478	200	91
8 (13)	0520334	4104971	130	130	525	240	139
9 (3a)	0523728	4098645	15	18	119	60	15
9 (3)	0518752	4098441	31	29	125	80	26
9 (7)	0517210	4099084	45	42	240	100	53
9 (10)	0515619	4099905	68	71	340	125	-
9 (11)	0514704	4100423	76	75	410	-	-
9 (12)	0513557	4101144	91	93	478	200	-
10 (3)	0519260	4094329	26	25	125	80	-
10 (7)	0517321	4095976	38	33	240	100	-
10 (10)	0516110	4096899	61	59	340	125	-
10 (12)	0515678	4096690	76	76	478	200	-
10 (13)	0515151	4096420	103	104	525	240	-
11 (3a)	0529880	4095212	14	16	119	60	14
11 (3)	0529261	4095438	27	28	125	80	27
11 (5)	0528919	4095511	32	31	200	-	-
11 (7)	0528518	4095580	38	38	240	100	40

Table 4: *All mapped inner edges from DEM and fieldwork with age assigned via synchronous correlation are shown. Note that all UTM coordinate are projected in 33 S grid zone. Note that not all the locations for inner edges mapped by DEMs analysis have been checked with GPS in the field*

because the investigated area is in places thickly-vegetated and densely-populated with private properties. However, see Figure 8 for a check of consistency between the two databases.

Figure captions

Figure 1: *(a), (b) and (c) Tectonic maps and cross-section showing late Quaternary to present deformation for Sicily and Calabria. The light blue-coloured dashed square shows the investigated area lying in the HP. Black and purple dots show the location of historical earthquakes; yellow dots show values of Holocene uplift rates from Antonioli et al. (2006). In (b) a sketched cross-section shows (i) the seismicity distribution and the Moho discontinuity along the transect A-B adapted from Chiarabba and Palano, (2017). In (c) rates of uplift mapped within the Calabrian Arc domain are shown from Ferranti et al. (2006).*
VF: Vibo Fault; TrF: Tropea Fault; MF: Mileto Fault; SeF: Serre Fault; CoF: Coccorino Fault; SEF: Sant'Eufemia Fault; SF: Scilla Fault; CF: Cittanova Fault; AF: Armo Fault; RCF: Reggio Calabria Fault; MTF: Messina-Taormina Fault; CDF; Capo D'Orlando Fault; WF: Western Fault; STTZ: Southern Tyrrhenian Thrust Zone; SLG: Scordia-Lentini Graben; ME: Malta Escarpment

Figure 2: *Location maps for palaeoshorelines within the HP, SE Sicily. A 2-m resolution DEM with the associated shaded-relief to highlight breaks of slope is used as base-map. Dashed coloured lines represent the inner edge of successive mapped palaeoshorelines. Locations where corals for U/Th dating have been collected and where available age controls from dated submerged palaeoshorelines used in this paper are shown. Numbered black lines indicate the 12 topographic profiles within the investigated area. Numbered dots represent inner edges location for palaeoshorelines, detailed in Table 4. Note that only 30 out of 50 km are shown for the offshore Western Fault (solid red line). The entire fault length is shown in Figure 1.*

Figure 3: *(a) and (b) Field photos showing the geomorphology of two successive palaeoshorelines with mapped inner edges along Profile 8, shown in Figure 2. In (c), (d) and (e) field evidence are presented for a palaeoshoreline, showing a scarp-like palaeocliff with the presence of lithophagid borings, and an associated limestone-made wave-cut platform with presence of mill-holes confirming wave action.*

Figure 4: *Field photos showing the sample location for a dated coral colony. The top photo shows an overview of where the coral colony was sampled for U/Th age determination, with a sketch stratigraphic log. Bottom photo shows details of the coral colony in-situ.*

Figure 5: *Results of synchronous correlation investigation of uplift rates. Root Mean Square deviation values are calculated for each topographic profile for all uplift scenarios from 0 to 1mm/yr at intervals of 0.05 mm/yr in order to show the best fit between "measured" and "predicted" palaeoshorelines elevations. The RMS values illustrate the misfit between measured and predicted palaeoshoreline elevations during iteration of the uplift rate. The uplift-rate with the lowest RMS misfit is preferred (refer to Figures 6 and 7 for visualisation of individual profiles).*

Figure 6: *(a) Topographic Profile 11 (see profile location in Figure 2) showing palaeoshoreline elevations predicted by synchronous correlation. (b) Palaeoshoreline elevations through time relative to the sea-level curves of Siddall et al. (2003). (c), (d) and (e) A synchronous correlation approach is applied driven by ages assigned to the submerged palaeoshorelines in order to find the best match between "measured" and "predicted" elevations. Note that some sea level highstands like 175 ka and 217 ka are lower than the next younger highstand, suggesting they may well be overprinted, that is,*

removed by erosion during rising sea-level during the subsequent highstand. (f) Table showing derived values.

Figure 7: *Profiles showing mapped and modelled palaeoshoreline elevations. The topographic profiles are from the 2 m DEM. The numbers with arrows mark the elevations of palaeoshorelines mapped in the field. The coloured lines indicate palaeoshoreline elevations (or former sea level highstand elevations) predicted by an uplift rate that has been changed iteratively to produce the best match with the mapped palaeoshorelines; goodness of fit is indicated by the value for the R^2 value in Figure 5 and RMS values in Figure 5. Profile locations shown in Figure 2.*

Figure 8: *(a) Linear regression analysis shows the relationship between field-based and DEM-based inner edge elevation measurements. The R^2 value > 0.99 confirms a strong correlation suggesting that elevations measured from the DEM are likely to be accurate. (b) Linear regression analysis between our measured and predicted palaeoshoreline elevations. The predicted elevations, representing the synchronously-calculated former sea-level highstand elevations, indicate a constant uplift rate through time, that has been derived by iterating this value to find the best match to the measured and mapped palaeoshorelines. Note that "measured" elevations represent palaeoshoreline elevations mapped in the 2-m high resolution DEMs. Coefficient of determination, R^2 value, has been used between these two datasets to quantify the best fit for Profiles 1-10, with a value > 0.99.*

Figure 9: *(a) Differential uplift from south to north of late Quaternary palaeoshorelines with palaeoshoreline ages derived in this study. (b) Values for uplift-rate increase from south to north along the N-S oriented transect. (c) Tilt angle values calculated for each mapped palaeoshoreline in (a), showing that older palaeoshorelines have higher tilt angles, suggesting that they have experienced a longer history of differential uplift, and that differential uplift has been ongoing progressively during the late Quaternary. Values of tilt angle for each investigated palaeoshoreline have been calculated, as a $\tan^{-1}$ of a gradient "m" of a straight-line equation (y=mx), as proposed by previous studies (Meschis et al., 2018; Robertson et al., 2019).*

Figure 10: *(a) Coseismic vertical displacements produced by the Western Fault suggested by half-elastic space modelling. The results indicate the extent to which footwall uplift affects the coastline of the HB. The model shows a simulated earthquake of Mw 7.05, produced if the entire length of the Western Fault (50 km) is ruptured with a slip at depth of 5.5m, with a dip-angle of 70°. (b) Assuming a recurrence interval of 500 years, because shorter intervals are not supported by the historical earthquake record (see text for discussion of this value), the footwall uplift-rate is <0.1 mm/yr, which does not explain the total uplift rate implied by the our determinations based on the elevations of late Quaternary palaeshorelines. The discrepancy between uplift-rates produced by footwall uplift and the total measured uplift-rate is indicated (double-headed black arrow), and this may reveal the magnitudes of uplift-rate produced by other processes.*

Figure 11: *Uplift rates obtained results from this paper (a-b) shown in the context of crustal thickening (c), the doming effects related to Etna (d), and horizontal GPS velocities (e). Higher values of uplift (a) and uplift rates (b) develop towards the north where deeper values of Moho discontinuity are mapped (c), higher values for uplift related to Etna (d), and lower values of horizontal GPS velocities approaching the thrust on the north side of the HP (e).*

Figure 12: *The relationship between uplift-rate and Moho depth. Regression analysis of values for uplift-rate and Moho depth reveal a power law relationship with an exponent of 1.86. This suggests that viscous deformation may be associated with the measured deformation.*

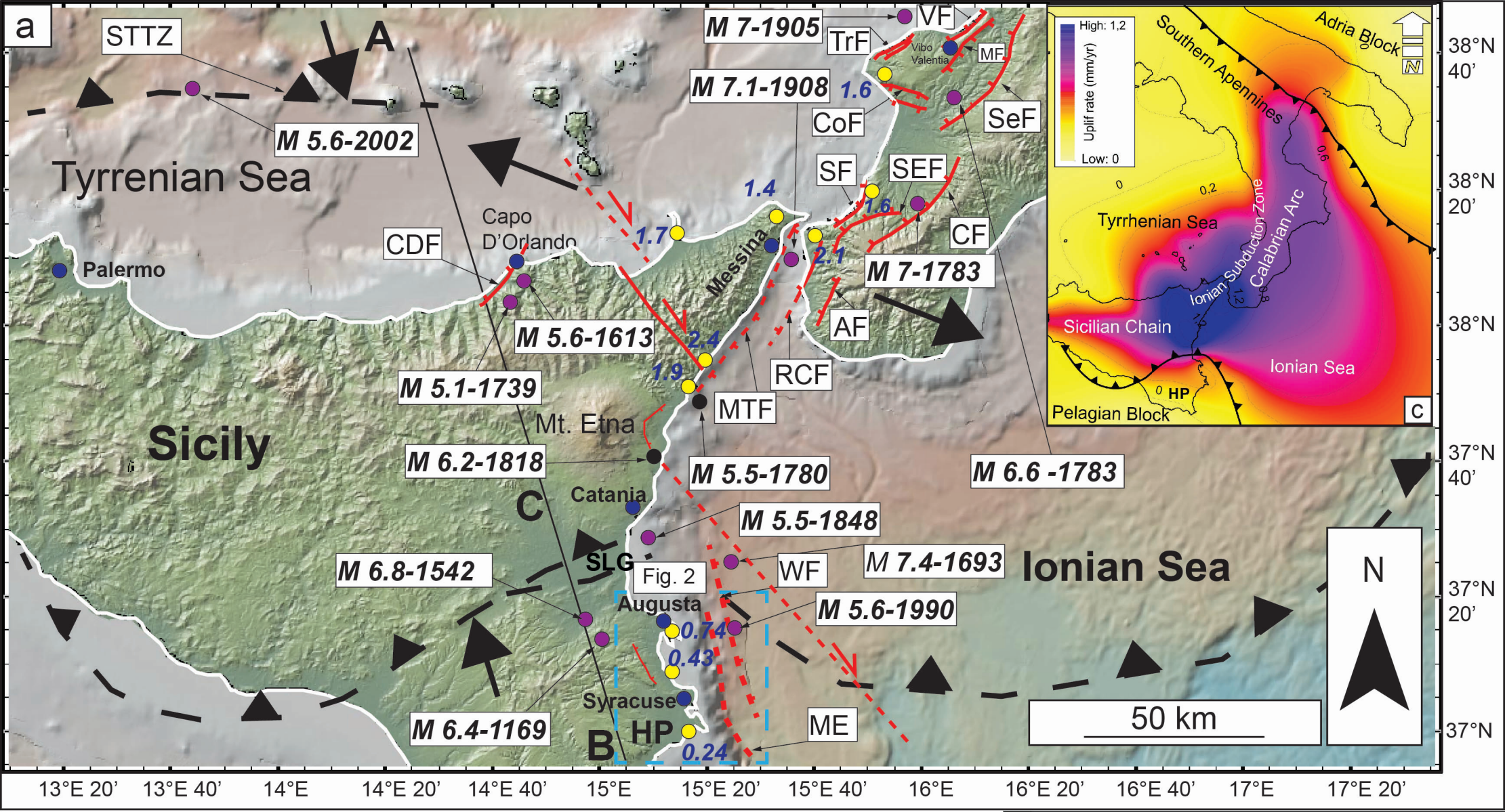

Recent and active normal faults (dashed in the offshore, ticks on the downthrown side)

Main Thrust

Historical Earthquakes Locations

M 7.1-1908

Magnitude (M) - Year of historical earthquakes

Holocene Uplift Rates (mm/yr) from Scicchitano et al. (2008) and Spampinato et al. (2011)

Town

Recent and active strike-slip faults (dashed in the offshore, arrows indicates lateral component of motion)

Direction of the regional extension

Direction of the Africa-Europe convergence

Study area

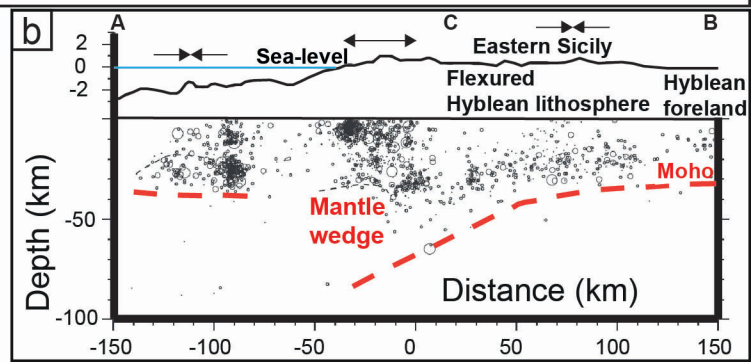

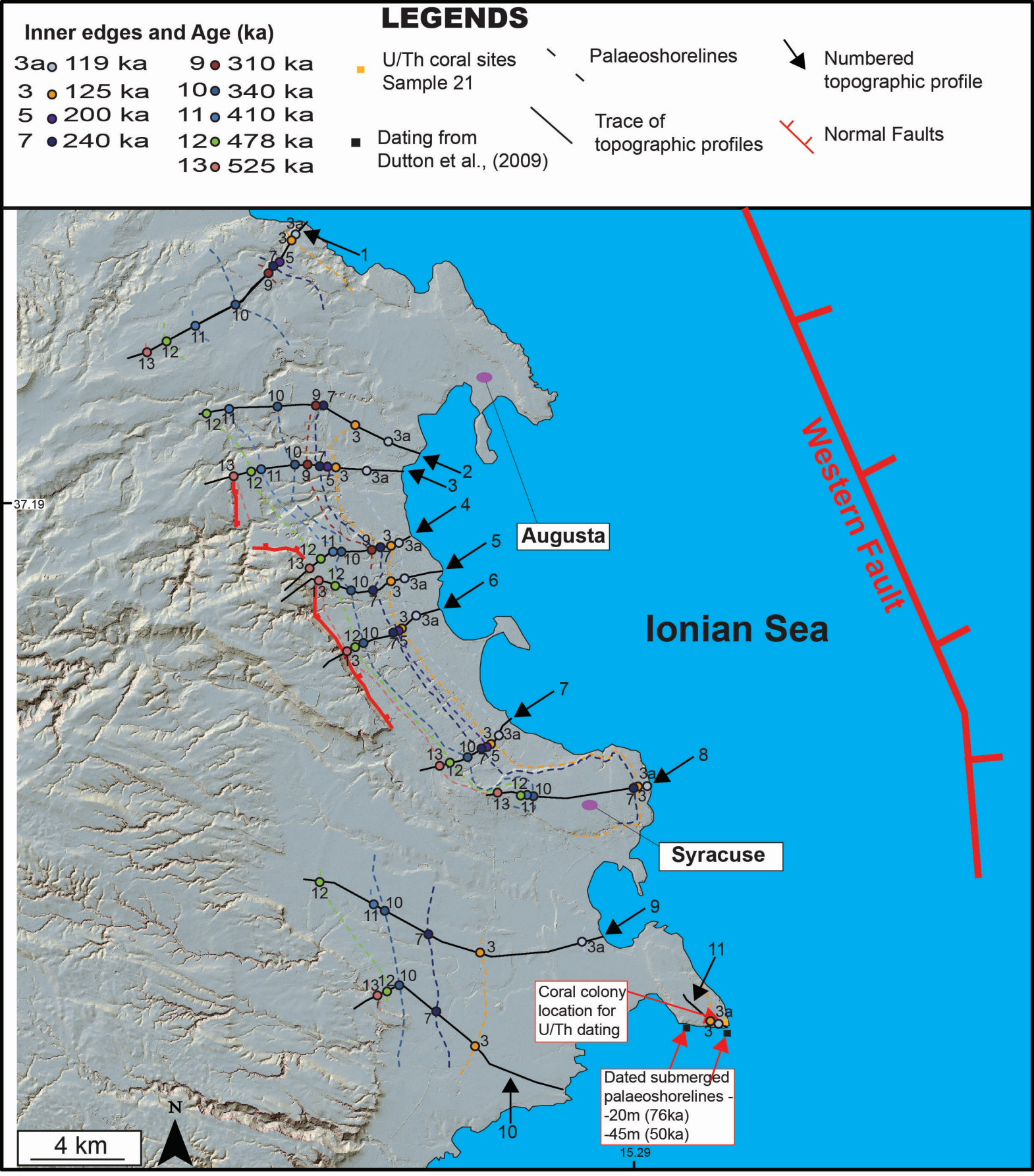
LEGENDS
Inner edges and Age (ka)
3a 119 ka
3 125 ka
5 200 ka
7 240 ka
9 310 ka
10 340 ka
11 410 ka
12 478 ka
13 525 ka
U/Th coral sites
Sample 21
Dating from
Dutton et al., (2009)
Palaeoshorelines
Trace of
topographic profiles
Numbered
topographic profile
Normal Faults
Western Fault
Ionian Sea
Augusta
Syracuse
Coral colony
location for
U/Th dating
Dated submerged
palaeoshorelines -
-20m (76ka)
-45m (50ka)
37.19
15.29
N
4 km

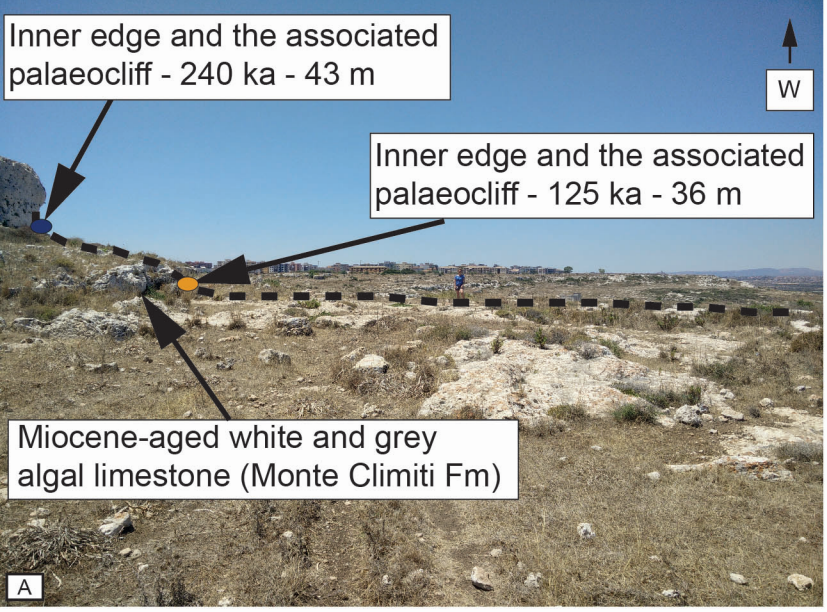
Inner edge and the associated palaeocliff - 240 ka - 43 m
W
Inner edge and the associated palaeocliff - 125 ka - 36 m
Miocene-aged white and grey algal limestone (Monte Climiti Fm)
A


B
S
240ka
125ka


C
N
Miocene-aged white and algal limestone
Lithophagid borings zone indicating the palaeo sea-level

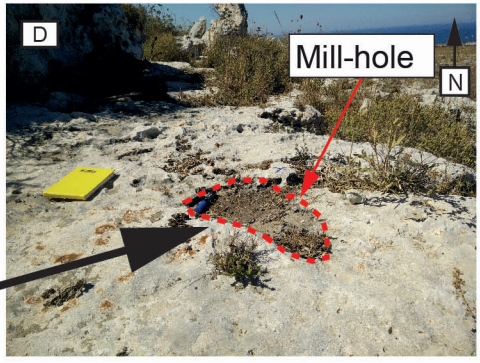
D
Mill-hole
N


E
Example of a lithophagid boring within the palaeocliff

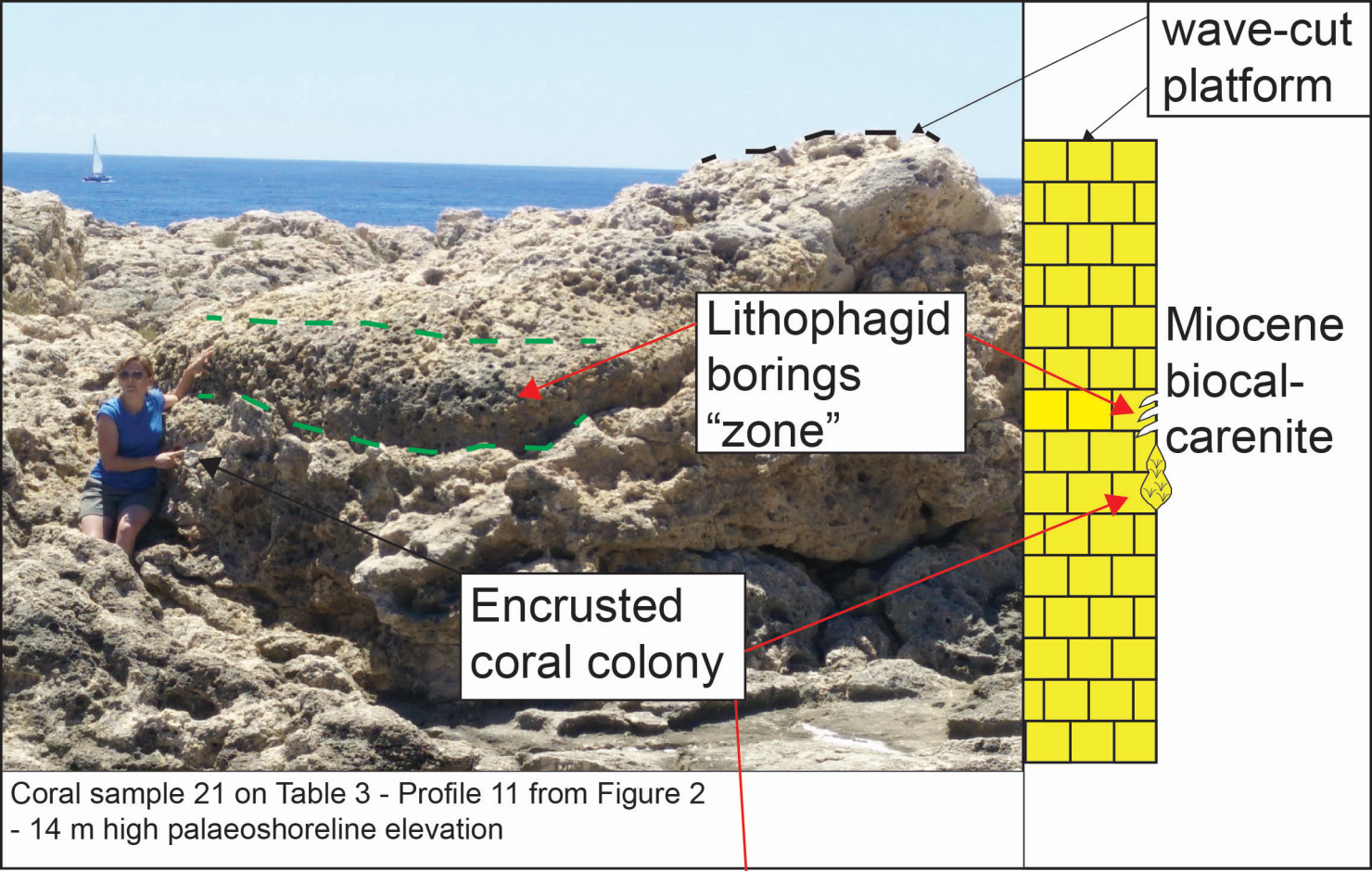

Coral sample 21 on Table 3 - Profile 11 from Figure 2 - 14 m high palaeoshoreline elevation

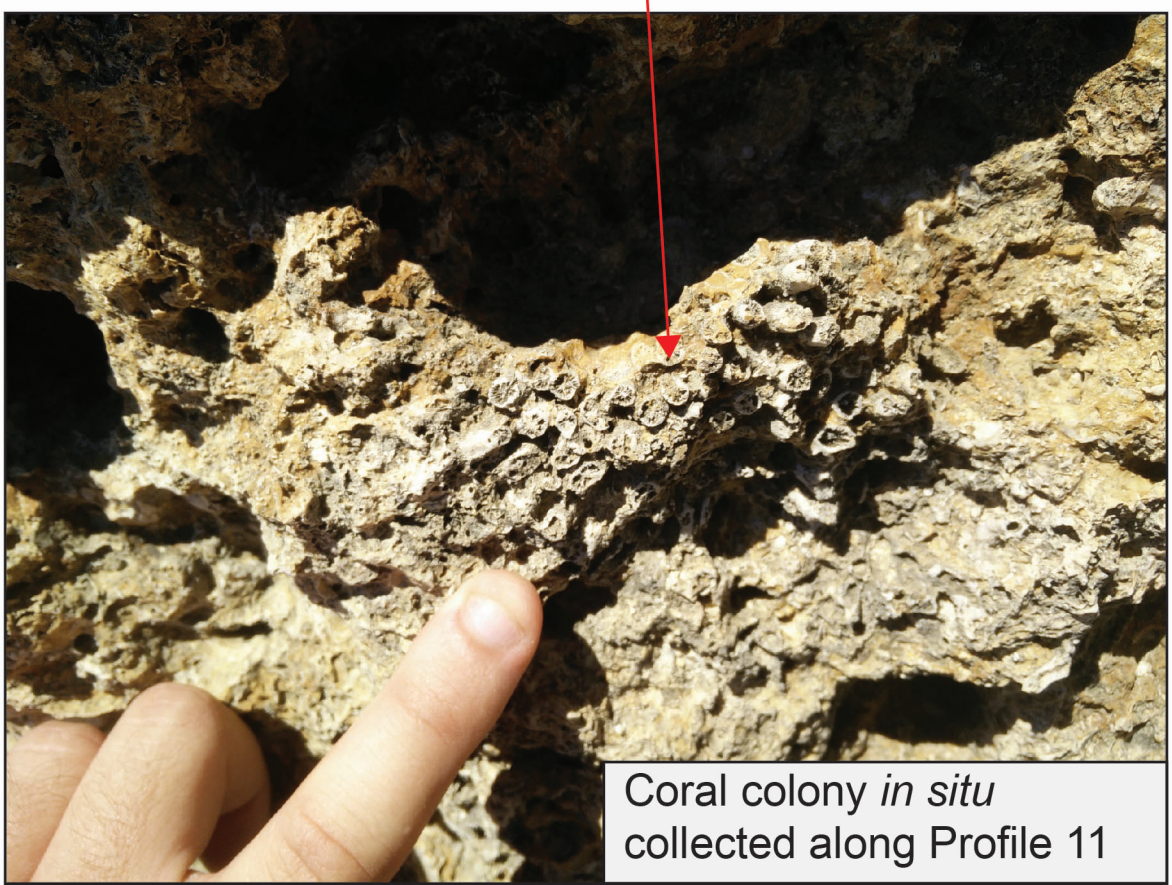

RMS Deviation vs Uplift rate (mm/yr)

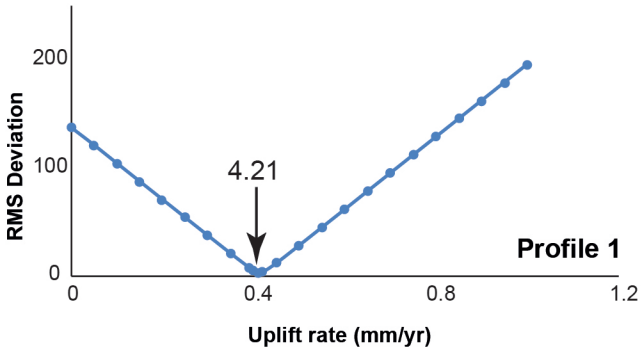

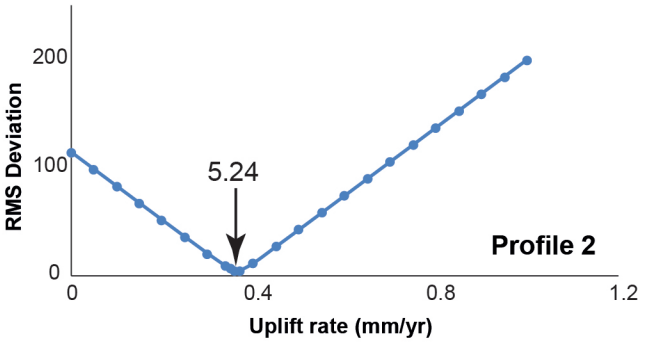

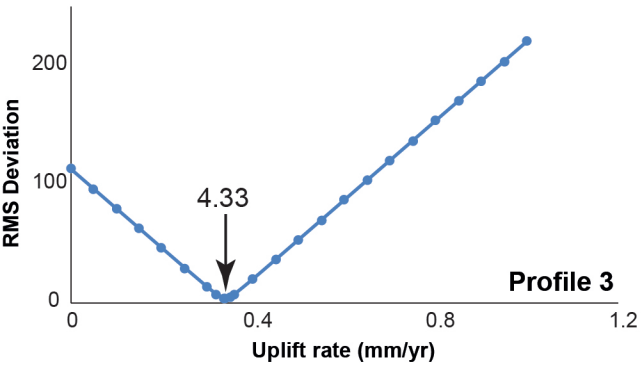

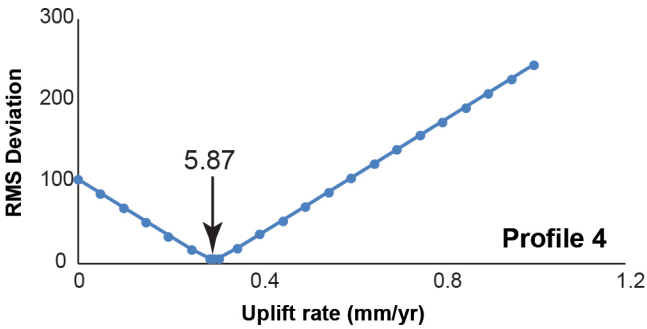

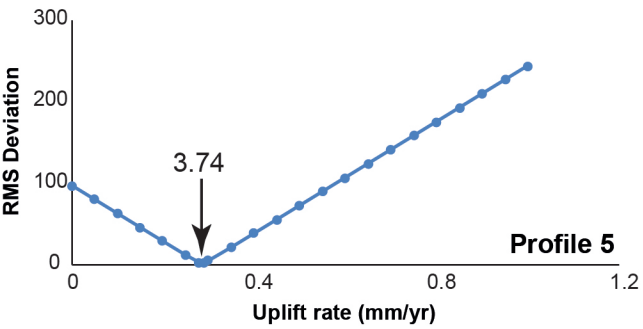

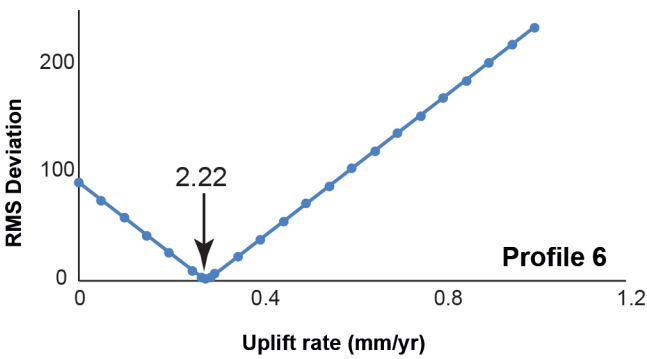

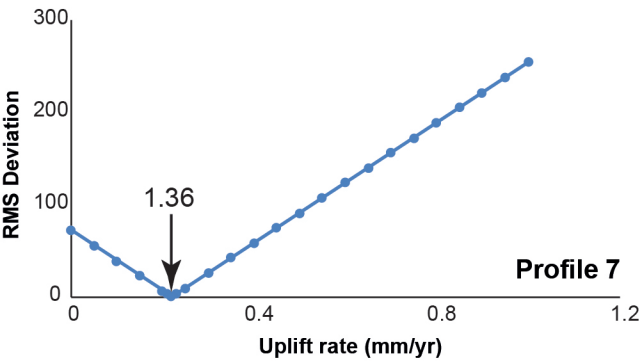

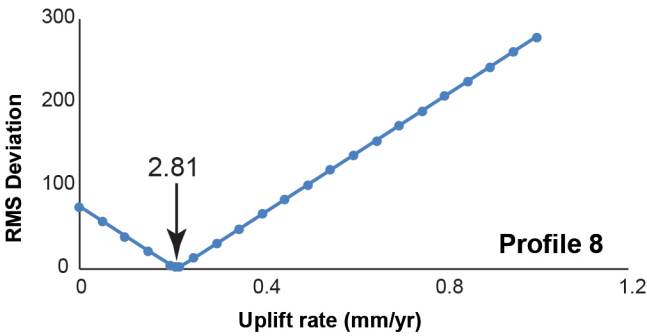

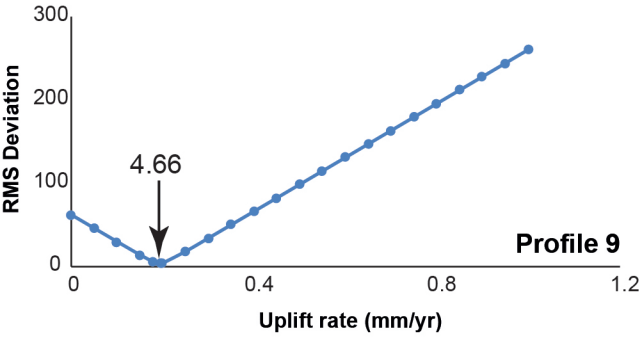

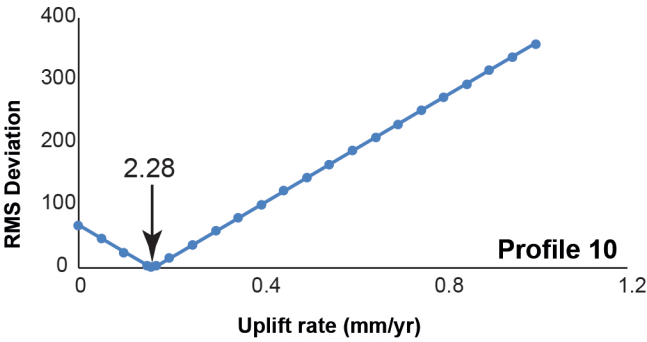

4.66 → RMS Deviation value

Topographic Profile 11 with modelled shoreline elevations

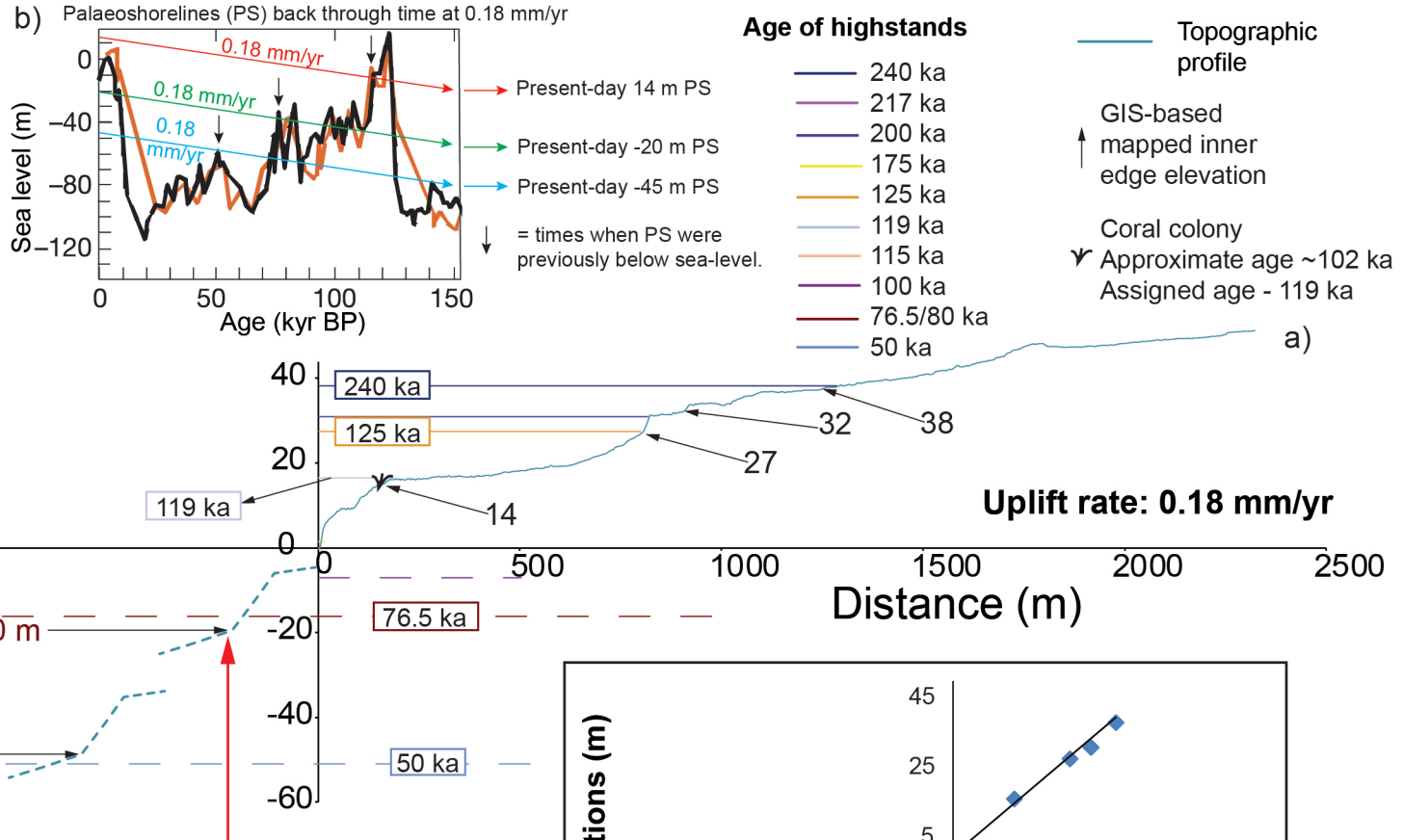

Modelled and sketched (not to scale) submerged palaeoshorelines dated by Dutton et al. (2009).

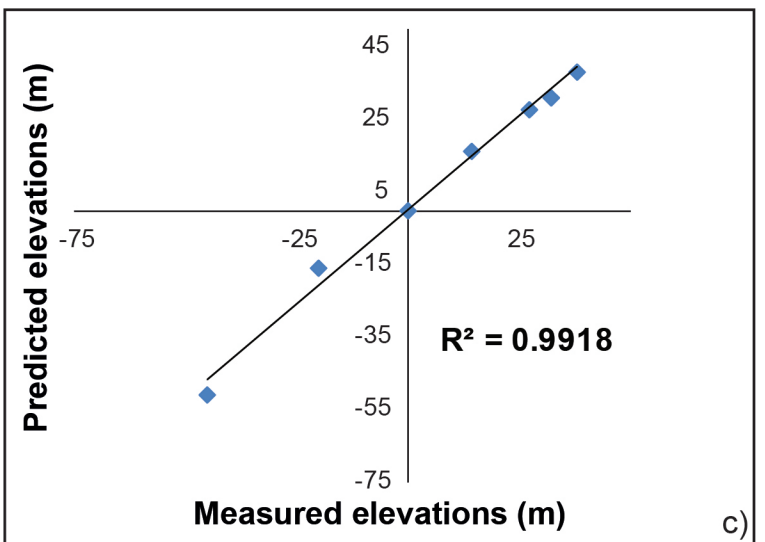

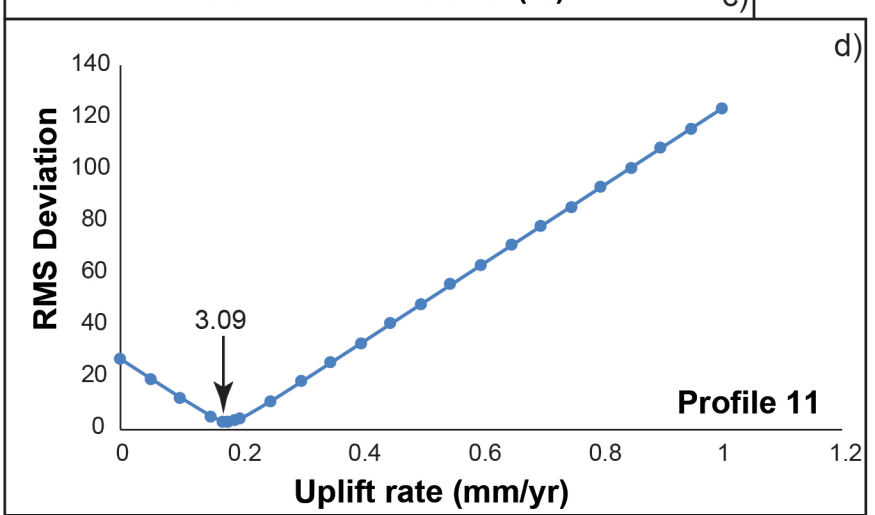

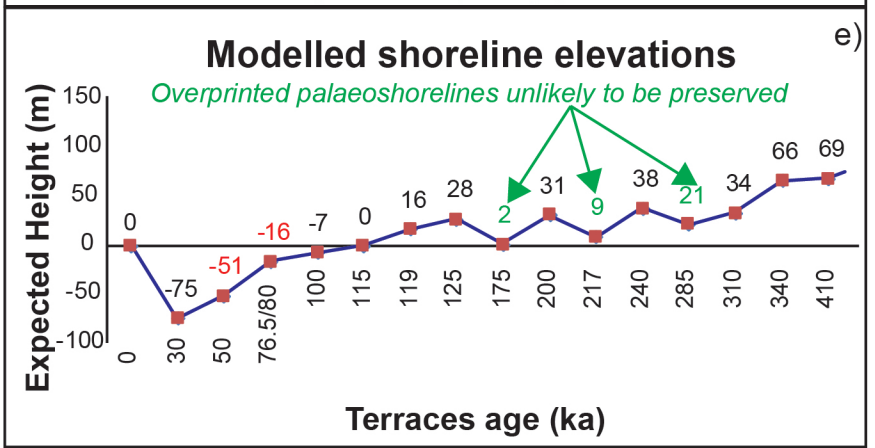

Uplift (mm/yr)	Highstands (ka)	Highstand elevations (m)	
		Predicted (Terrace Calc)	Measured (Field/DEM)
0.18	50	-51	-45
	76.5/80	-16	-20
	100	-7	-
	115	0	-
	119	16	14
	125	28	27
	175	2	-
	200	31	32
	217	9	-
	240	38	38

f)

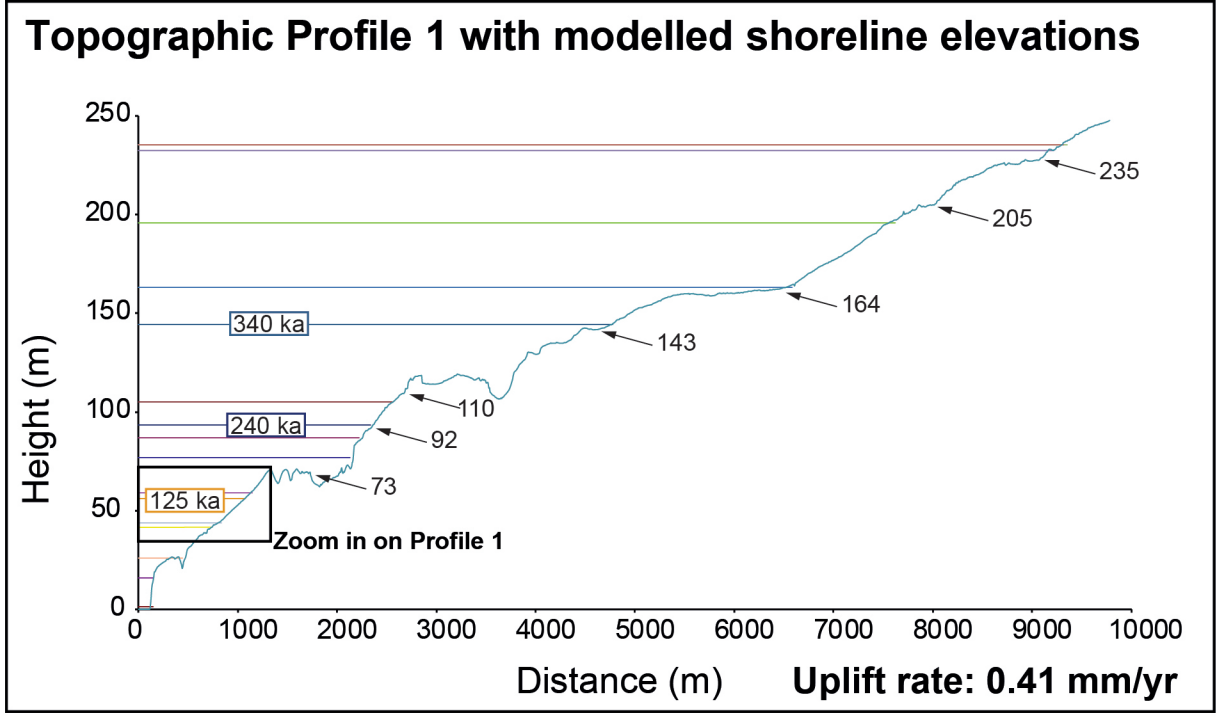

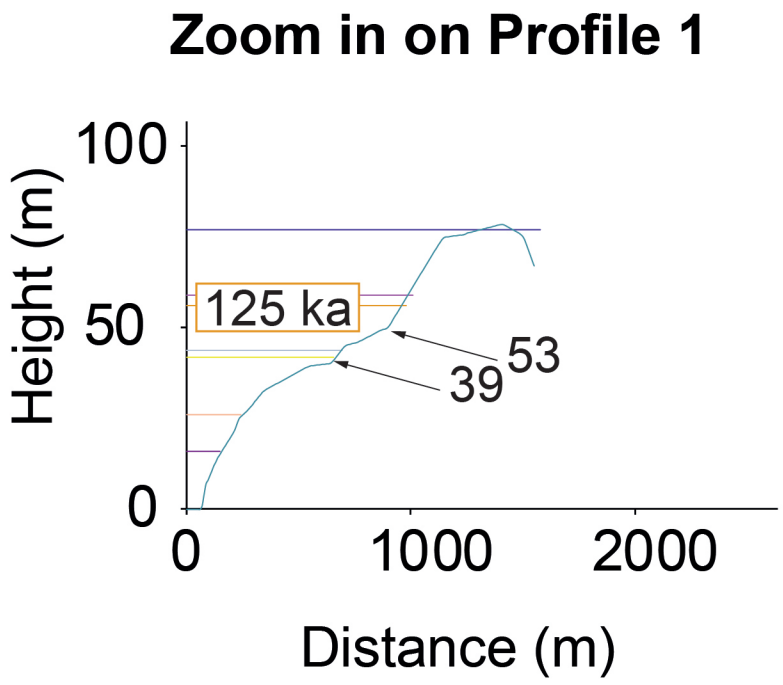

a)

980 ka | 620 ka | 478 ka | 240 ka | 119 ka | 30 ka
855 ka | 590 ka | 410 ka | 217 ka | 115 ka | Topographic profile
800 ka | 560 ka | 340 ka | 200 ka | 100 ka
740 ka | 550 ka | 310 ka | 175 ka | 76.5/80 ka | GIS-based mapped inner edge elevation
695 ka | 525 ka | 285 ka | 125 ka | 50 ka

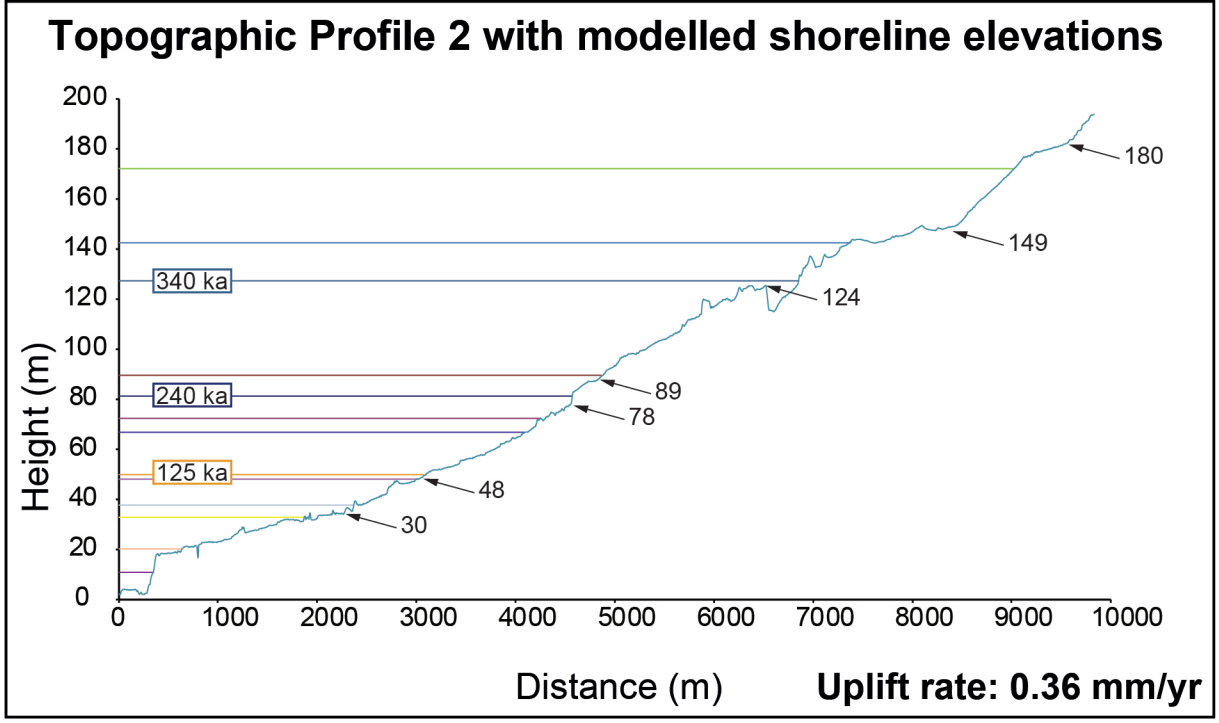

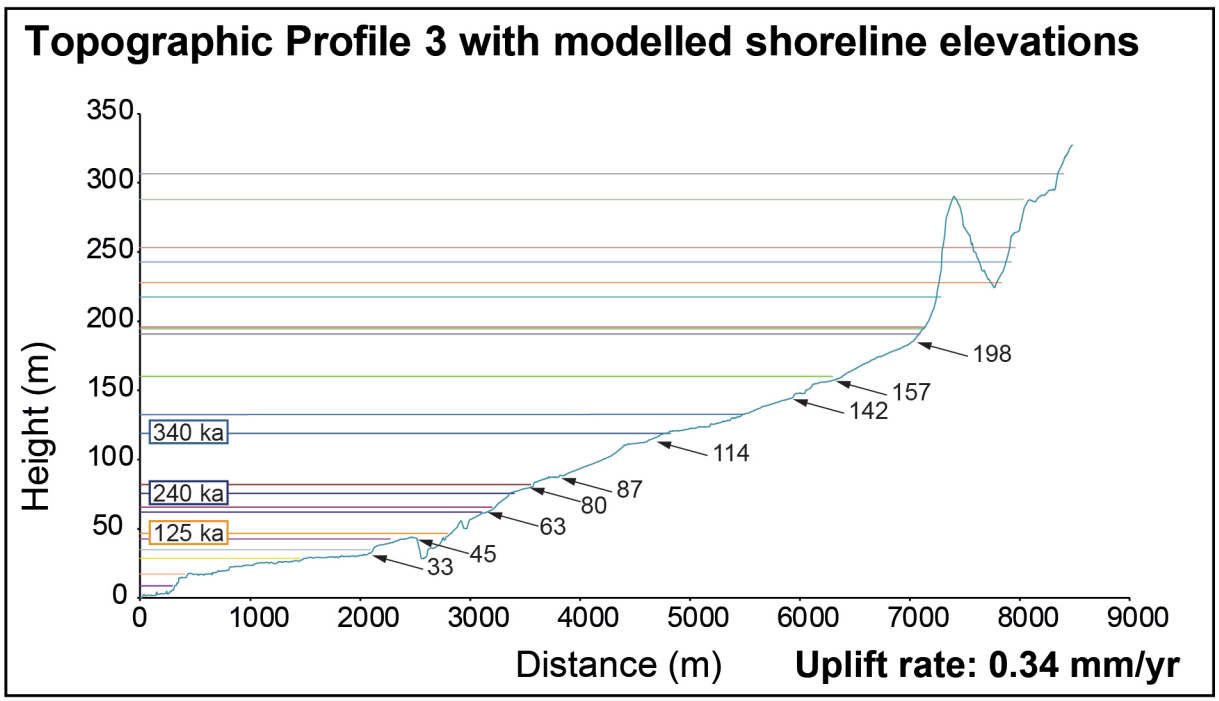

b)

980 ka
855 ka
800 ka
740 ka
695 ka
620 ka
590 ka
560 ka
550 ka
525 ka
478 ka
410 ka
340 ka
310 ka
285 ka
240 ka
217 ka
200 ka
175 ka
125 ka
119 ka
115 ka
100 ka
76.5/80 ka
50 ka
30 ka
Topographic profile
GIS-based mapped inner edge elevation

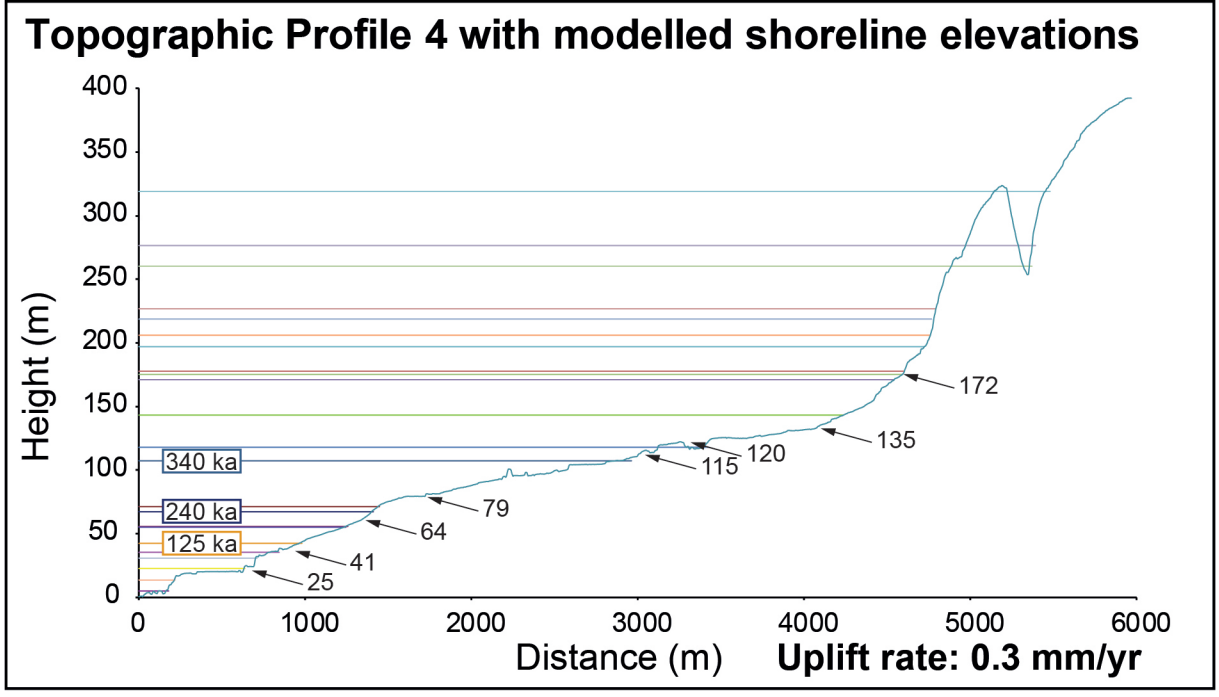

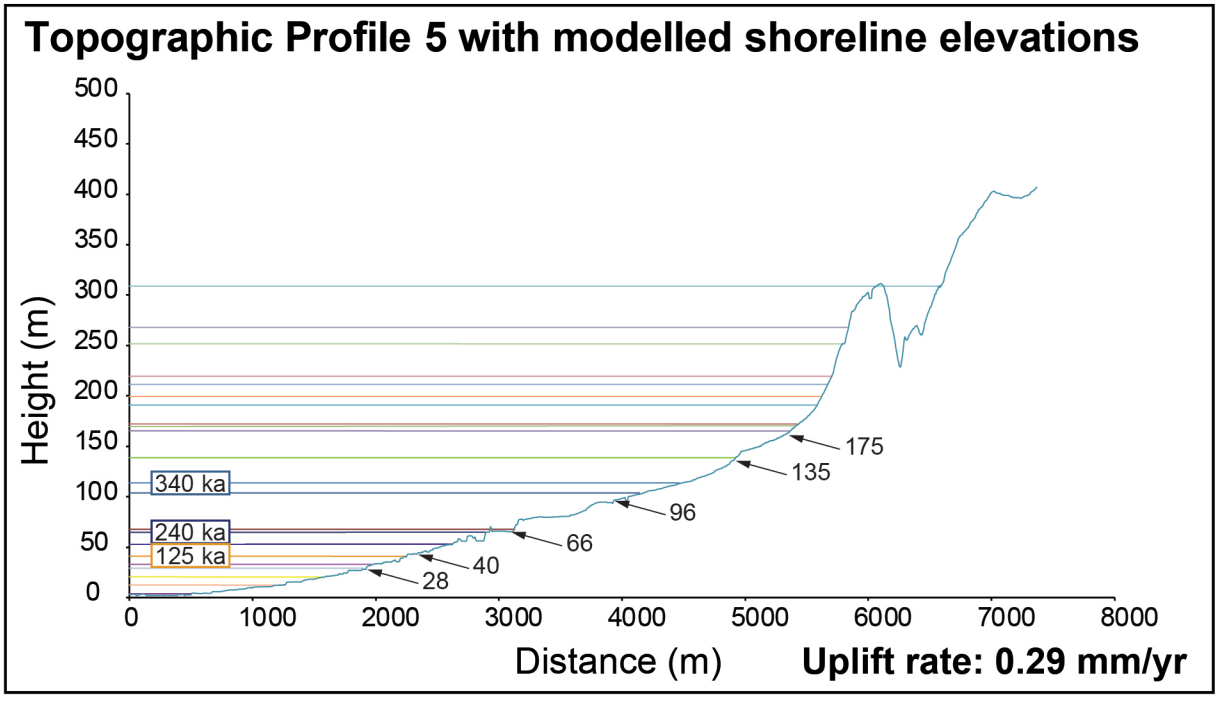

c)

980 ka | 620 ka | 478 ka | 240 ka | 119 ka | 30 ka
855 ka | 590 ka | 410 ka | 217 ka | 115 ka | Topographic profile
800 ka | 560 ka | 340 ka | 200 ka | 100 ka |
740 ka | 550 ka | 310 ka | 175 ka | 76.5/80 ka | GIS-based mapped inner edge elevation
695 ka | 525 ka | 285 ka | 125 ka | 50 ka |

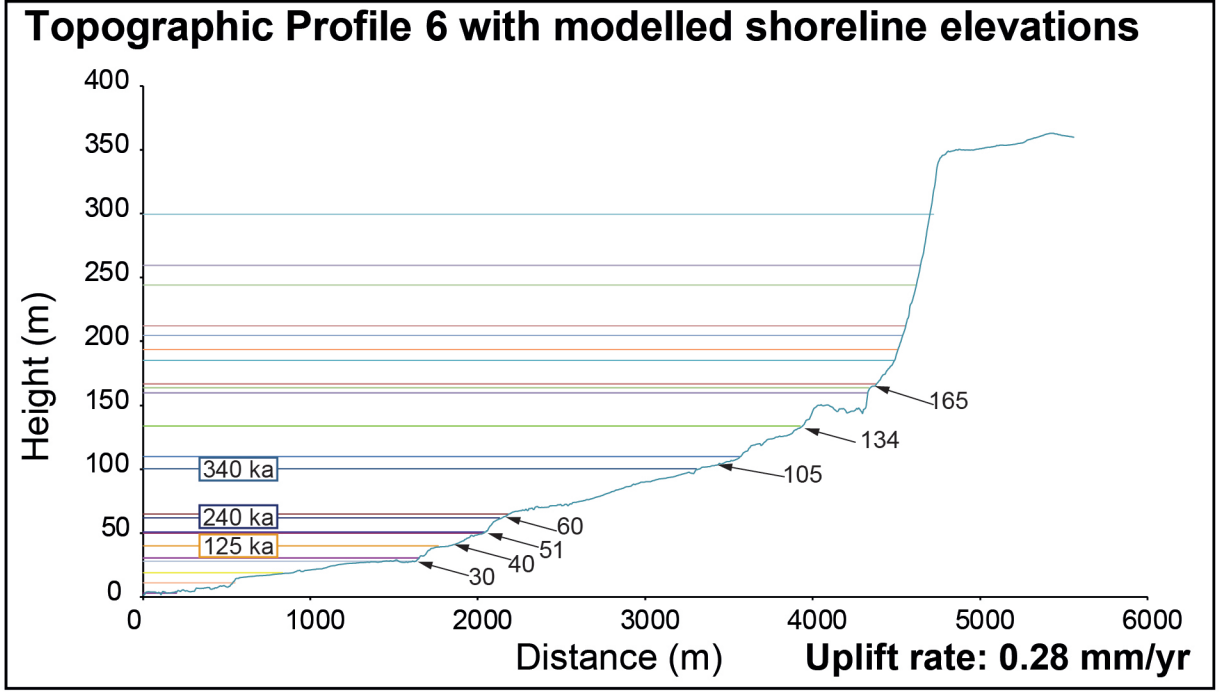

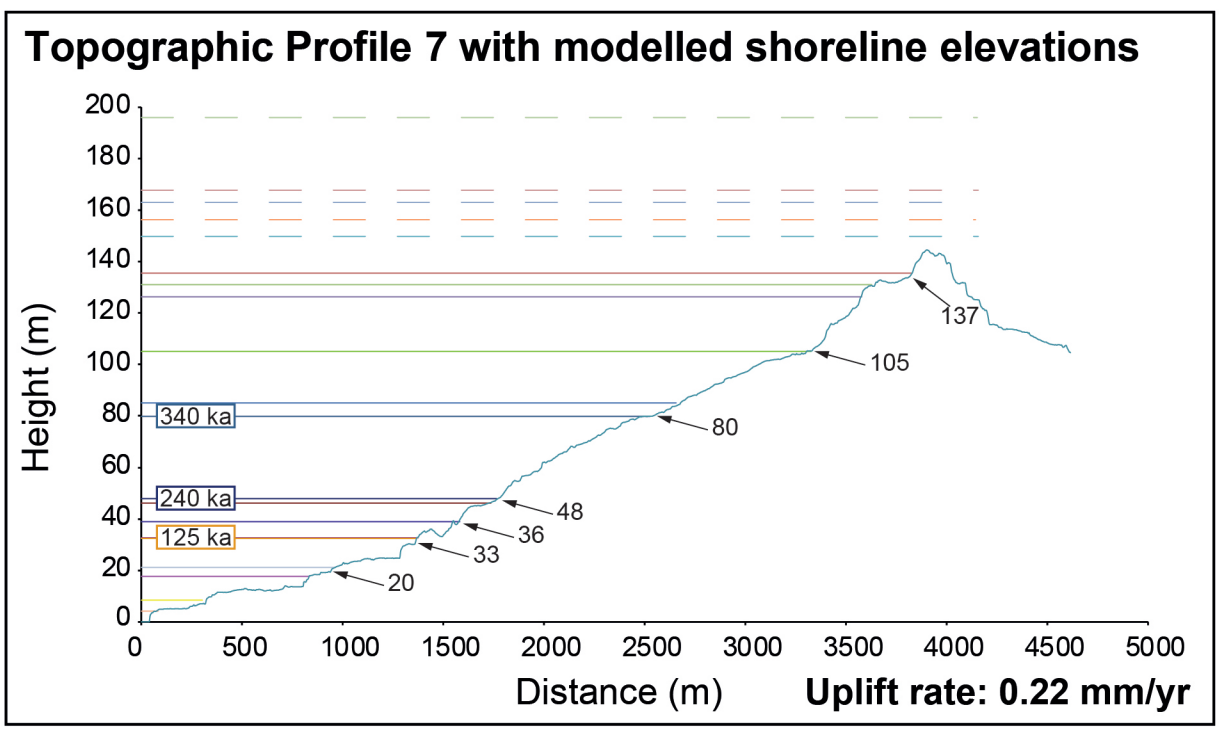

d)

980 ka
855 ka
800 ka
740 ka
695 ka
620 ka
590 ka
560 ka
550 ka
525 ka
478 ka
410 ka
340 ka
310 ka
285 ka
240 ka
217 ka
200 ka
175 ka
125 ka
119 ka
115 ka
100 ka
76.5/80 ka
50 ka
30 ka
Topographic profile
GIS-based mapped inner edge elevation

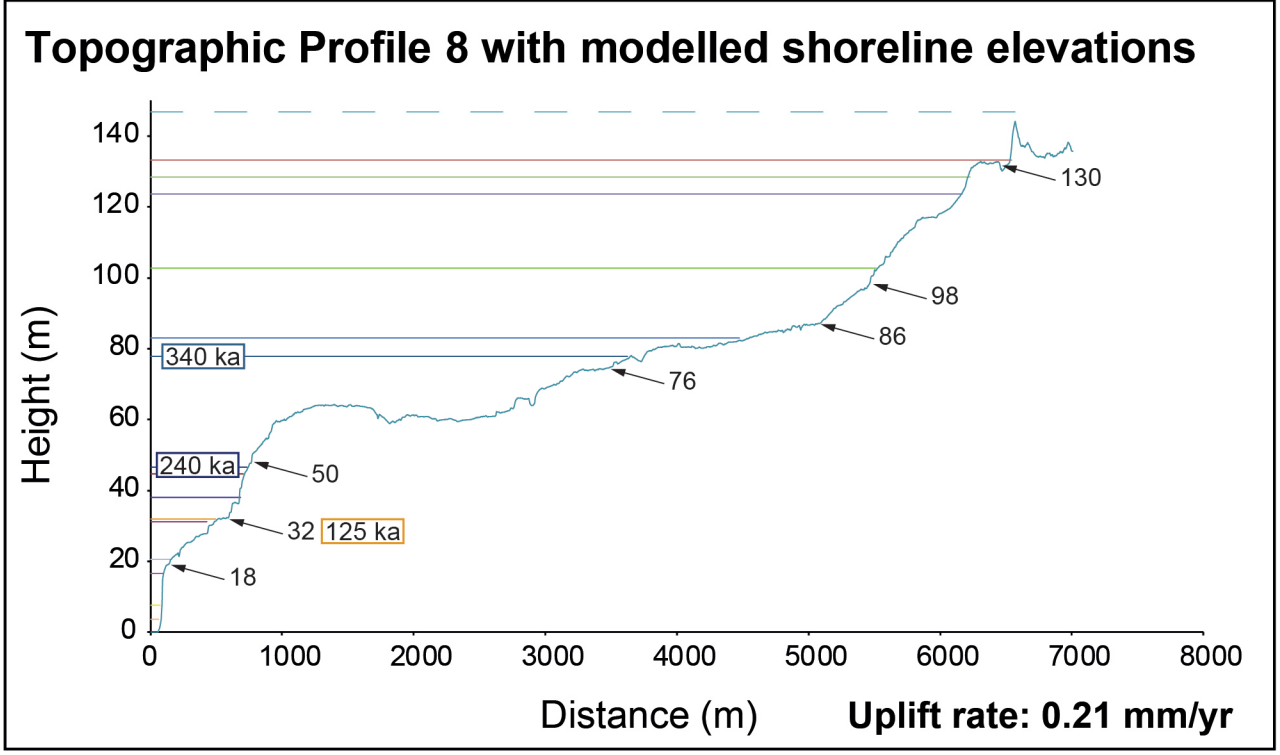

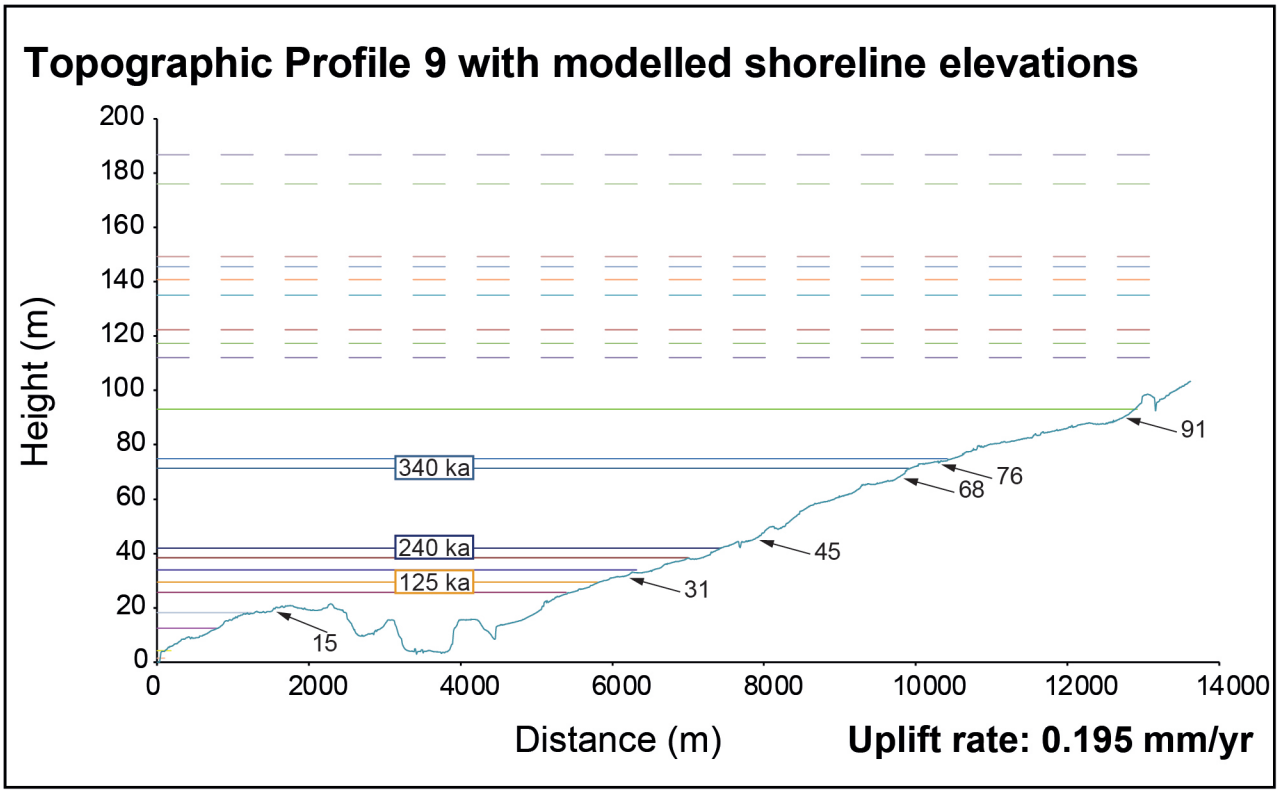

e)

980 ka | 620 ka | 478 ka | 240 ka | 119 ka | 30 ka

855 ka | 590 ka | 410 ka | 217 ka | 115 ka | Topographic profile

800 ka | 560 ka | 340 ka | 200 ka | 100 ka

740 ka | 550 ka | 310 ka | 175 ka | 76.5/80 ka | GIS-based mapped inner edge elevation

695 ka | 525 ka | 285 ka | 125 ka | 50 ka

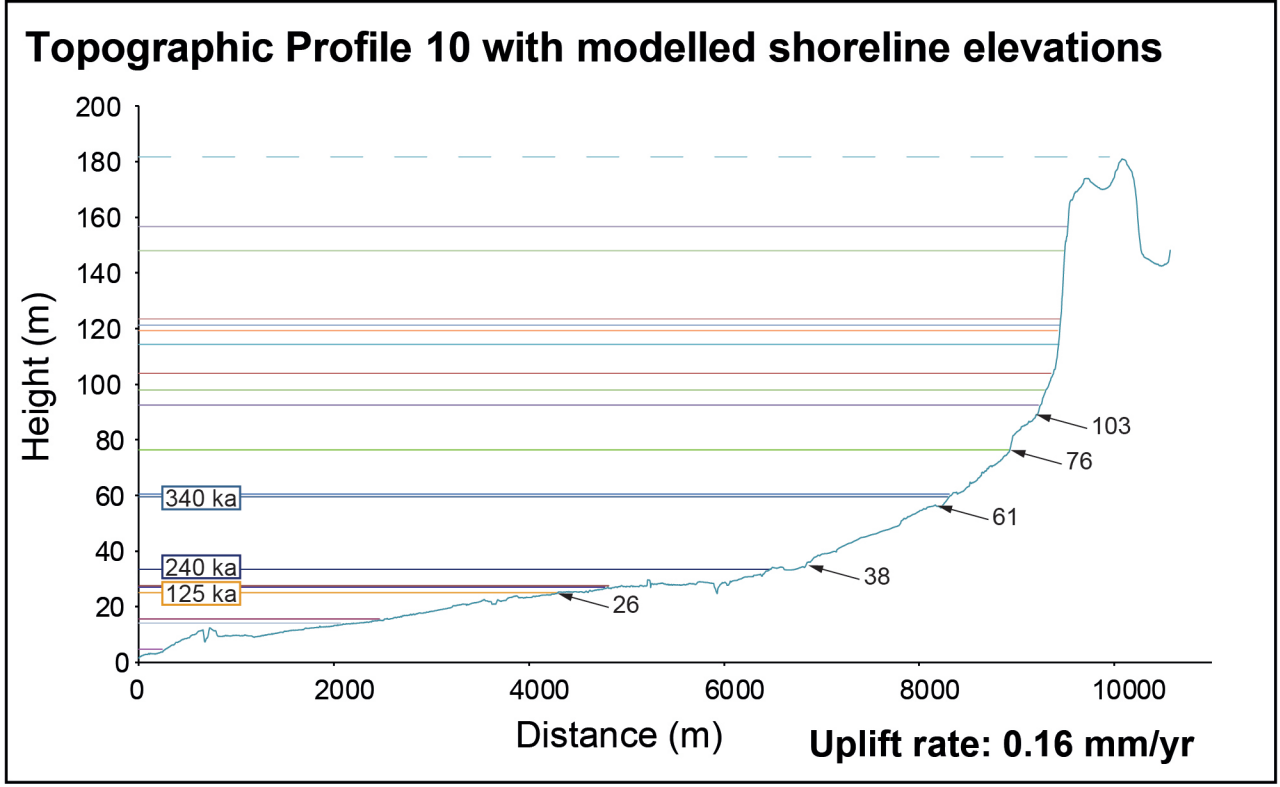

f)

980 ka
620 ka
478 ka
240 ka
119 ka
30 ka
855 ka
590 ka
410 ka
217 ka
115 ka
Topographic profile
800 ka
560 ka
340 ka
200 ka
100 ka
740 ka
550 ka
310 ka
175 ka
76.5/80 ka
GIS-based mapped inner edge elevation
695 ka
525 ka
285 ka
125 ka
50 ka

a)

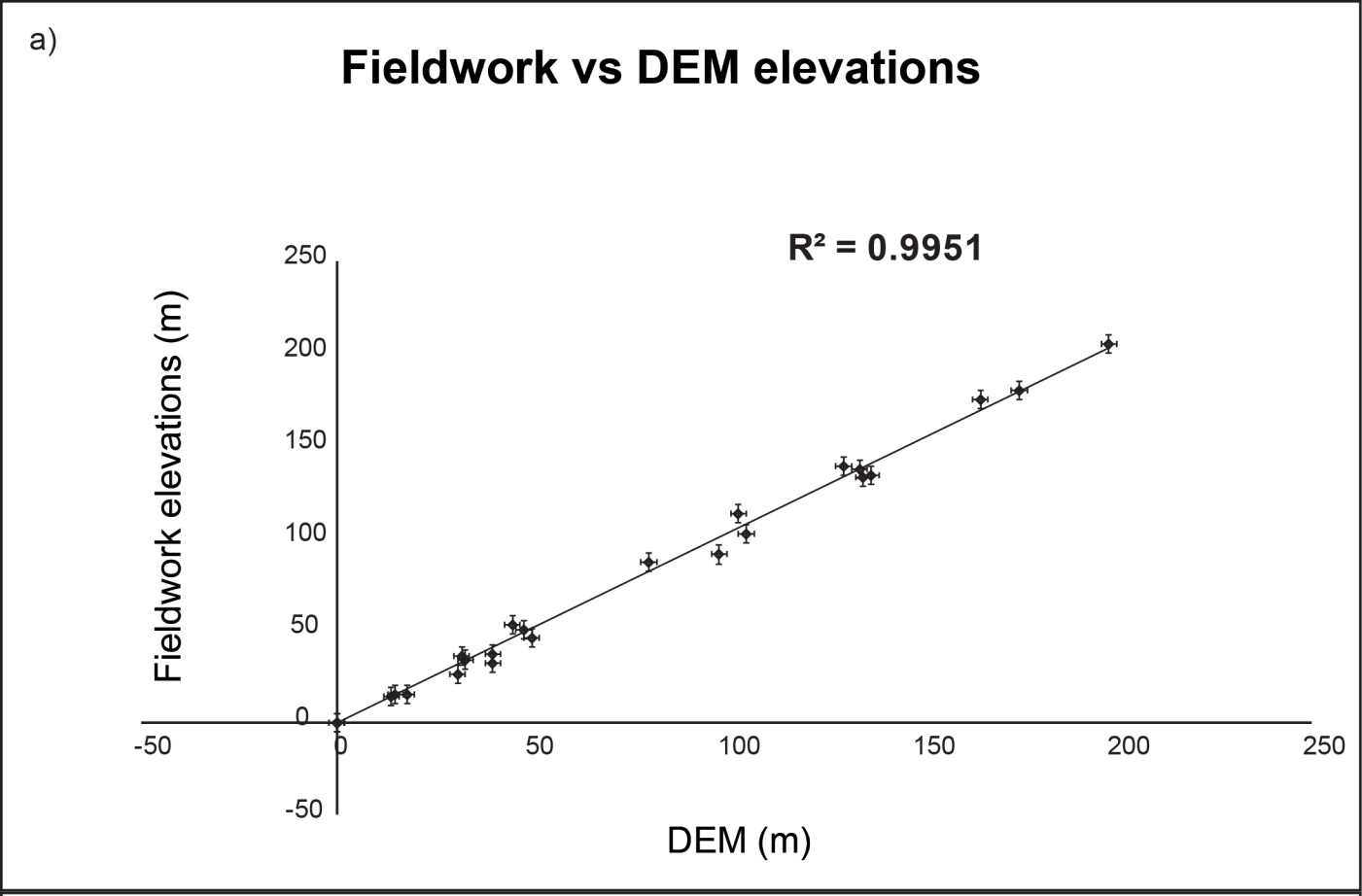
Fieldwork vs DEM elevations
R² = 0.9951
Fieldwork elevations (m)
DEM (m)
250
200
150
100
50
0
-50
-50
0
50
100
150
200
250

b)

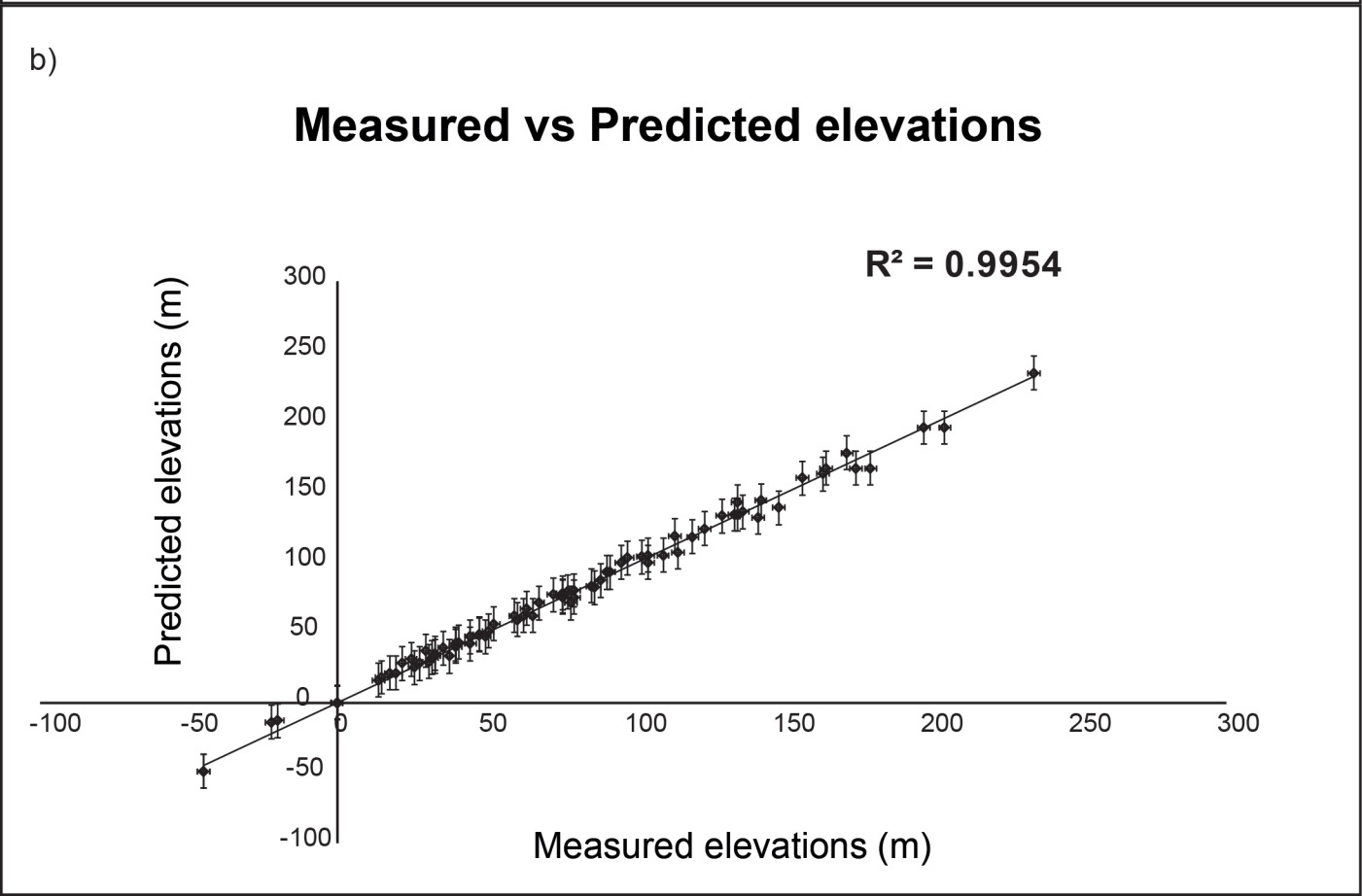
Measured vs Predicted elevations
R² = 0.9954
Predicted elevations (m)
Measured elevations (m)
300
250
200
150
100
50
0
-50
-100
-100
-50
0
50
100
150
200
250
300

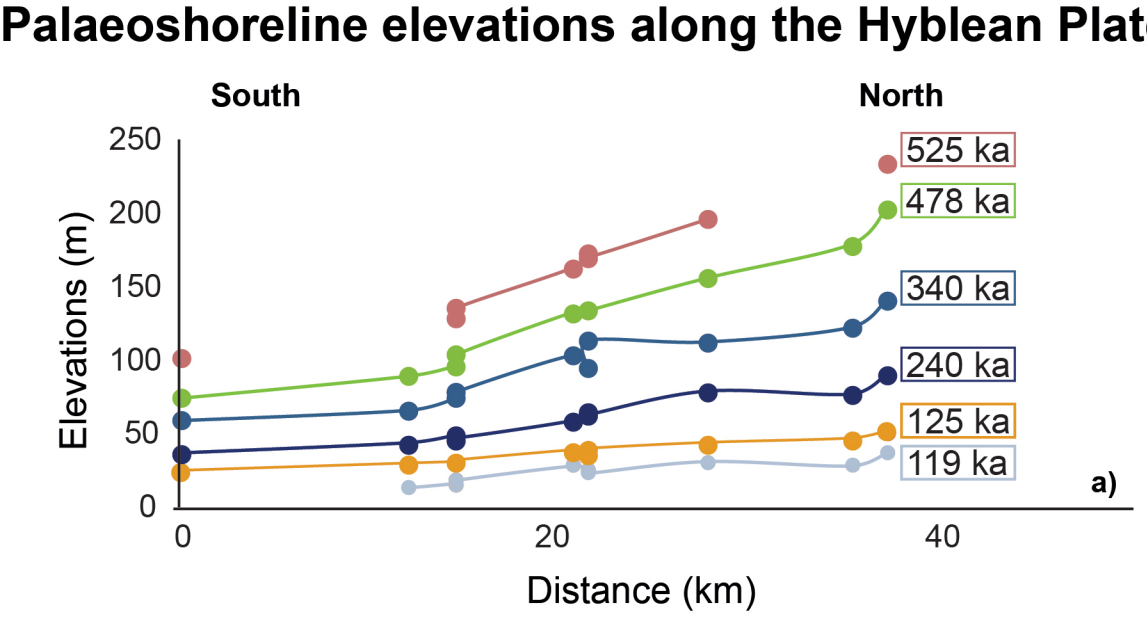
Palaeoshoreline elevations along the Hyblean Plateau
South
North
525 ka
478 ka
340 ka
240 ka
125 ka
119 ka
Elevations (m)
250
200
150
100
50
0
0
20
40
Distance (km)
a)

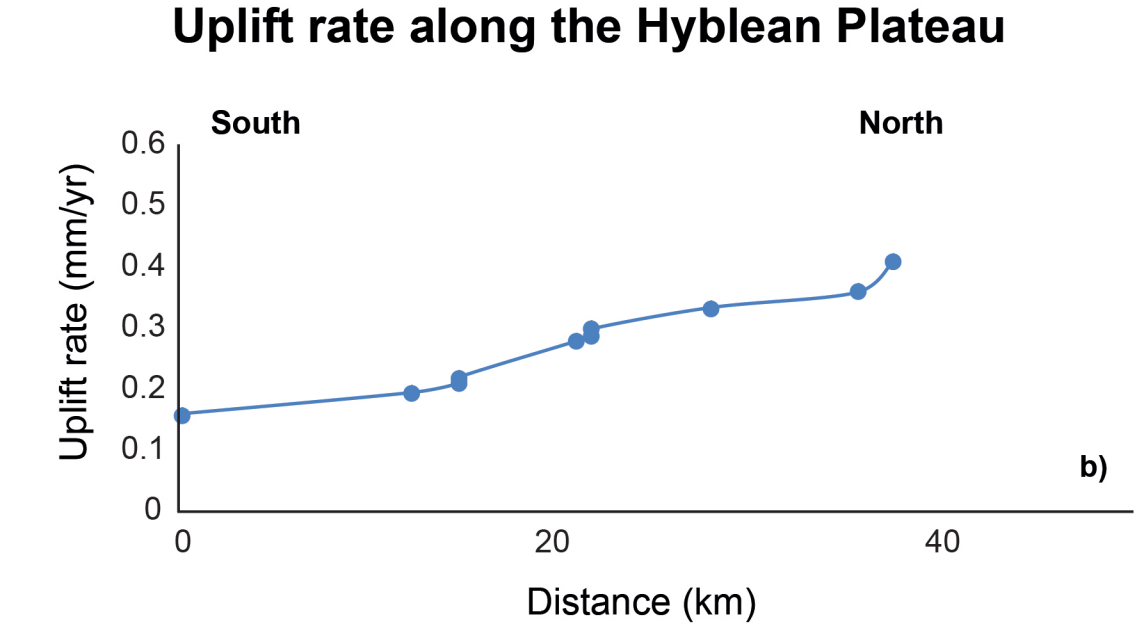
Uplift rate along the Hyblean Plateau
South
North
Uplift rate (mm/yr)
0.6
0.5
0.4
0.3
0.2
0.1
0
0
20
40
Distance (km)
b)

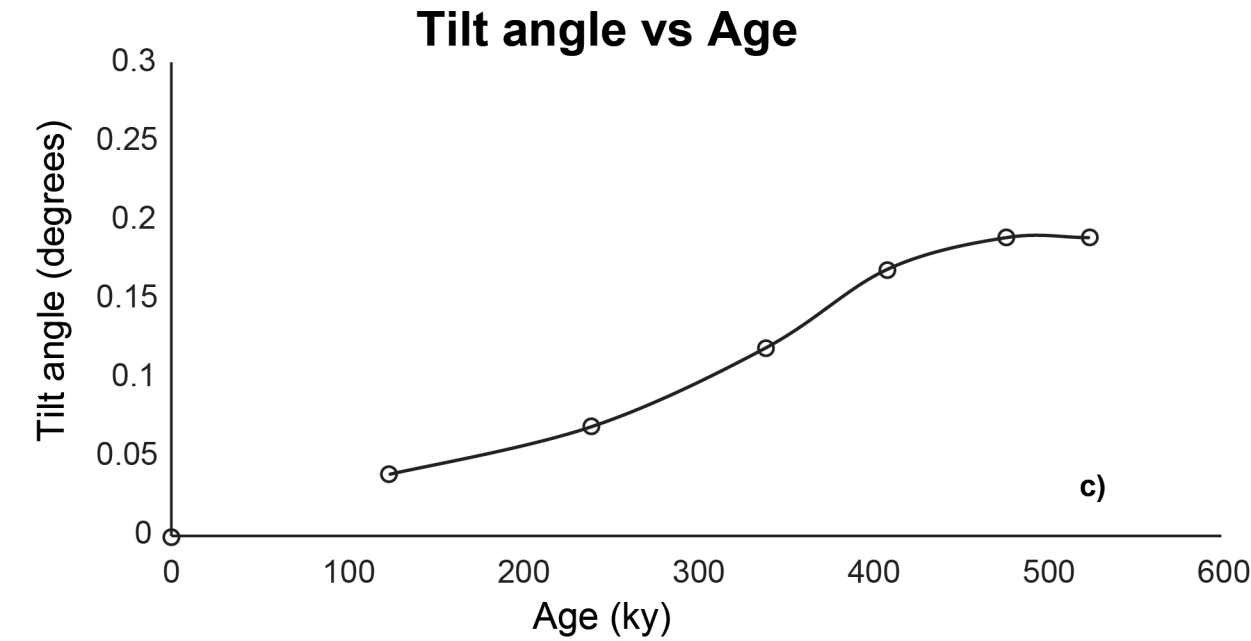
Tilt angle vs Age
Tilt angle (degrees)
0.3
0.25
0.2
0.15
0.1
0.05
0
0
100
200
300
400
500
600
Age (ky)
c)

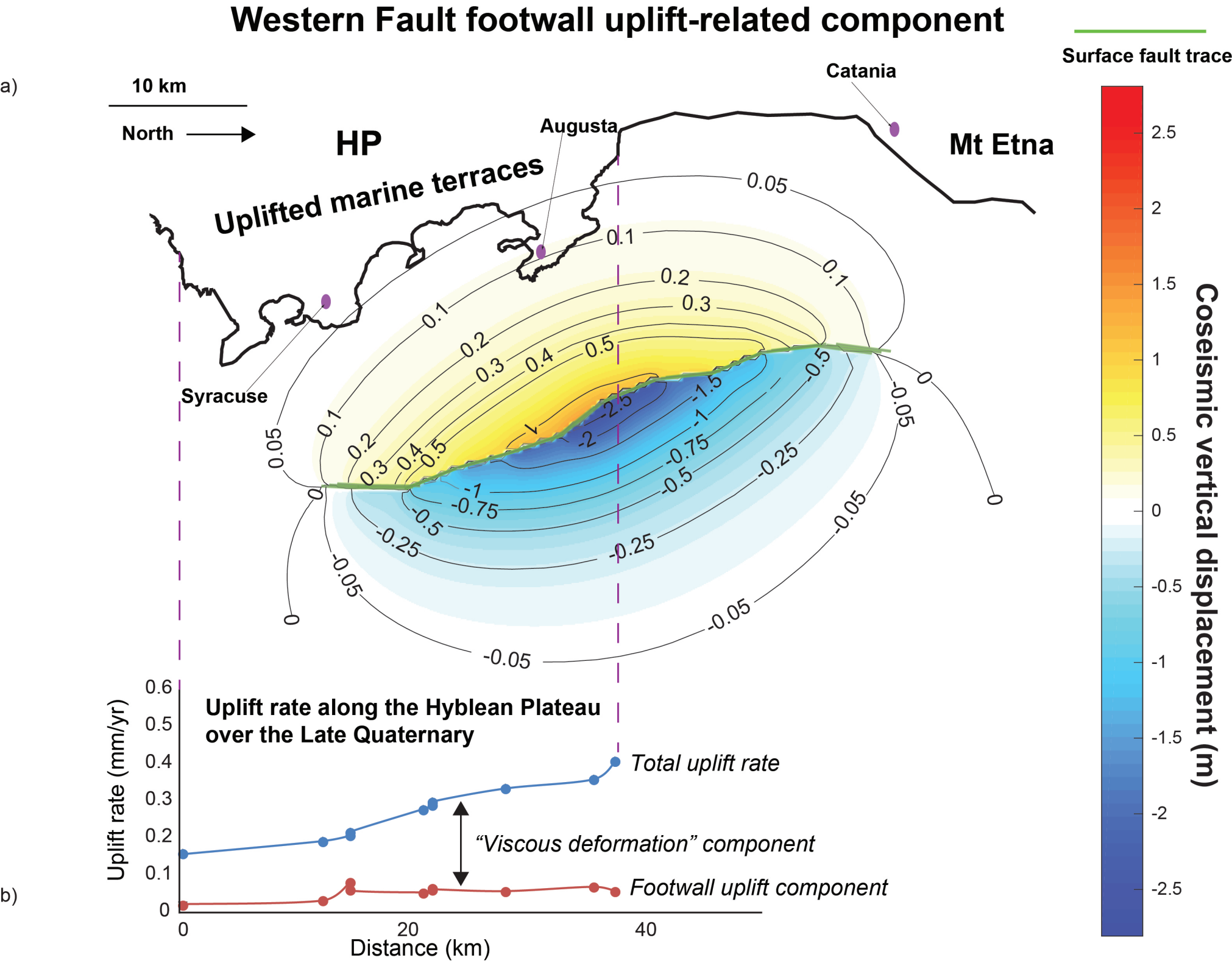
Western Fault footwall uplift-related component
Surface fault trace
a)
10 km
North
HP
Uplifted marine terraces
Augusta
Catania
Mt Etna
Syracuse
Coseismic vertical displacement (m)
2.5
2
1.5
1
0.5
0
-0.5
-1
-1.5
-2
-2.5
Uplift rate along the Hyblean Plateau over the Late Quaternary
Uplift rate (mm/yr)
Distance (km)
Total uplift rate
"Viscous deformation" component
Footwall uplift component
b)

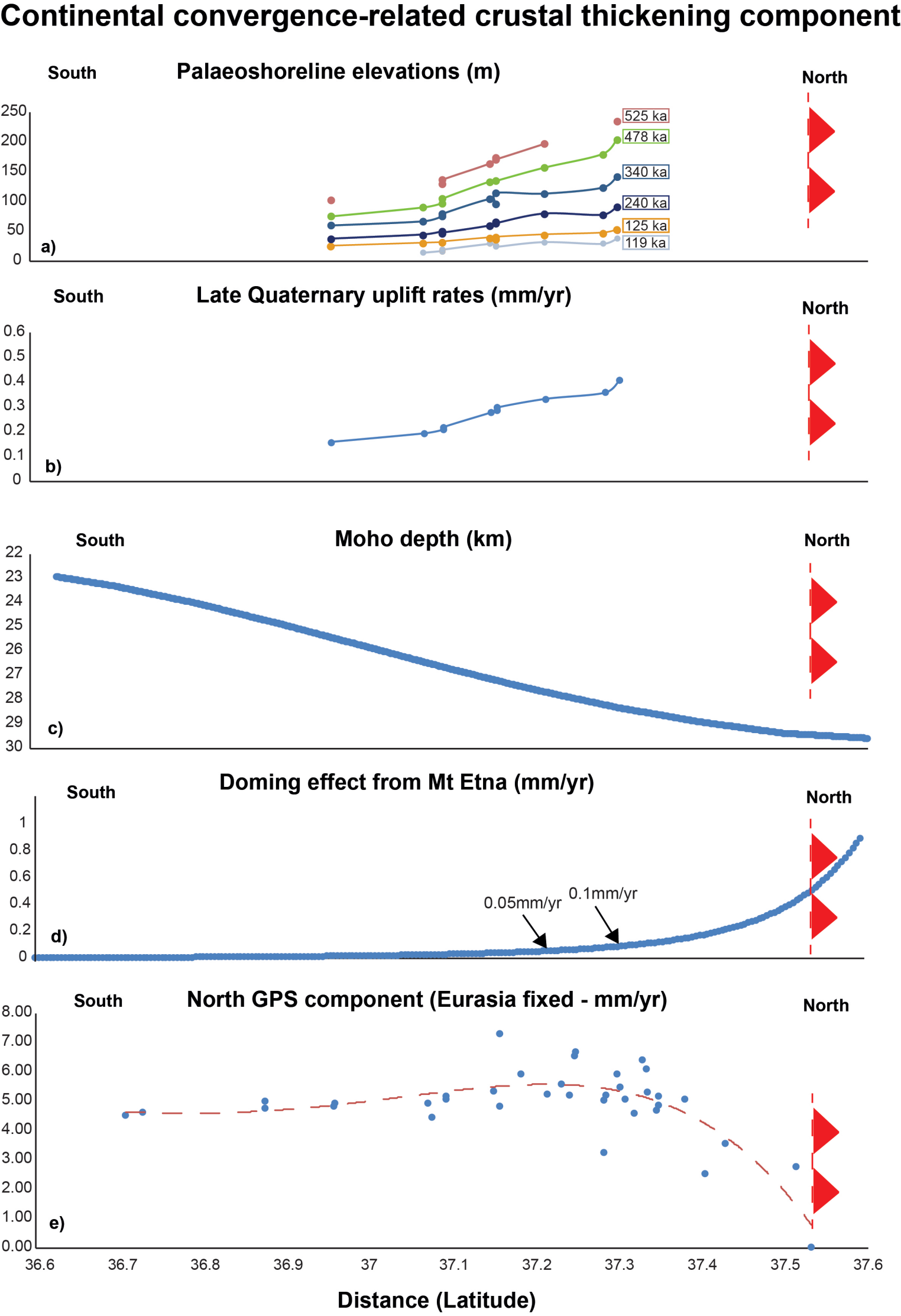
Continental convergence-related crustal thickening component
South
Palaeoshoreline elevations (m)
North
250
200
150
100
50
0
525 ka
478 ka
340 ka
240 ka
125 ka
119 ka
a)
South
Late Quaternary uplift rates (mm/yr)
North
0.6
0.5
0.4
0.3
0.2
0.1
0
b)
South
Moho depth (km)
North
22
23
24
25
26
27
28
29
30
c)
South
Doming effect from Mt Etna (mm/yr)
North
1
0.8
0.6
0.4
0.2
0
0.05mm/yr
0.1mm/yr
d)
South
North GPS component (Eurasia fixed - mm/yr)
North
8.00
7.00
6.00
5.00
4.00
3.00
2.00
1.00
0.00
e)
36.6
36.7
36.8
36.9
37
37.1
37.2
37.3
37.4
37.5
37.6
Distance (Latitude)

Uplift rate vs Moho depth

Uncorrected for FW uplift

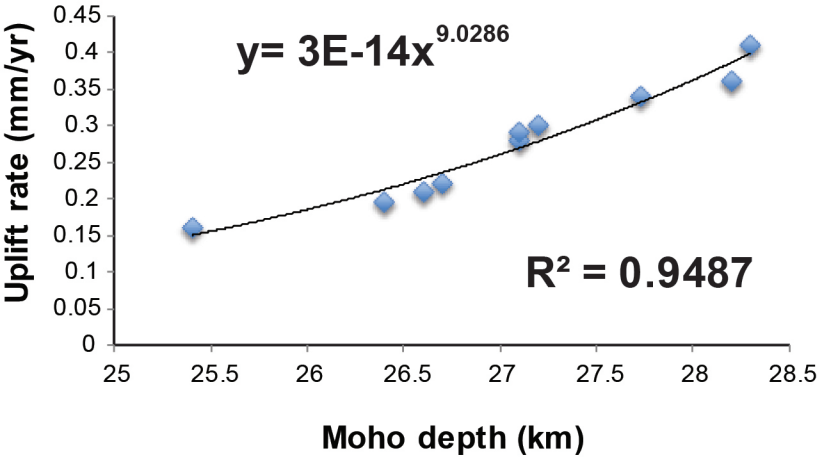

Uplift rate vs Moho depth log-log

Uncorrected for FW uplift

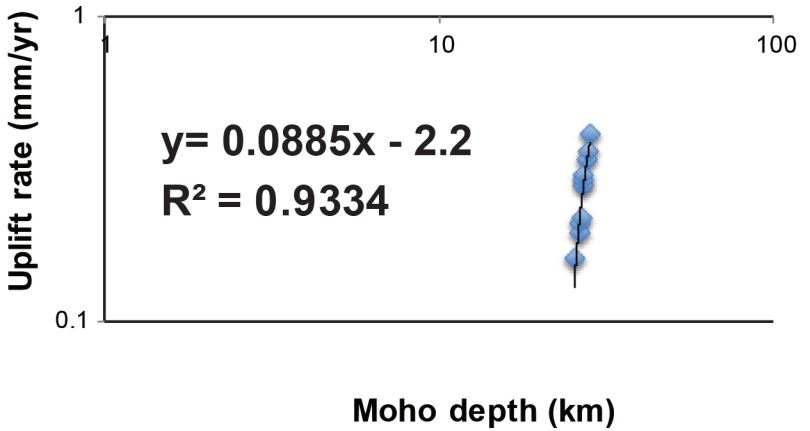

Uplift rate vs Moho depth

Corrected for FW uplift

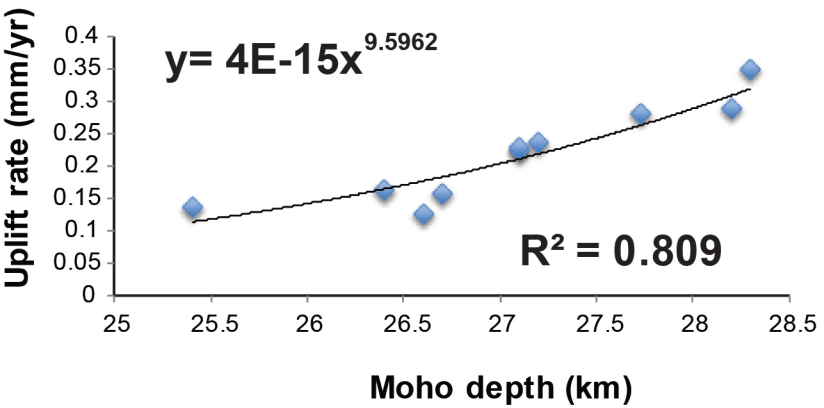

Uplift rate vs Moho depth log-log

Corrected for FW uplift